A&A, 690, A59 (2024)
https://doi.org/10.1051/0004-6361/202449822

Astronomy & Astrophysics

Dwarf galaxies as a probe of a primordially magnetized Universe

Mahsa Sanati[1,2,⋆], Sergio Martin-Alvarez[3], Jennifer Schober[1], Yves Revaz[1], Adrianne Slyz[2], and Julien Devriendt[2]

[1] Institute of Physics, Laboratory of Astrophysics, École Polytechnique Fédérale de Lausanne (EPFL), 1290 Sauverny, Switzerland
[2] Subdepartment of Astrophysics, University of Oxford, Keble Road, Oxford OX1 3RH, UK
[3] Kavli Institute for Particle Astrophysics & Cosmology (KIPAC), Stanford University, Stanford, CA 94305, USA

Received 29 February 2024 / Accepted 8 July 2024

ABSTRACT

Aims. The true nature of primordial magnetic fields (PMFs) and their role in the formation of galaxies remains elusive. To shed light on these unknowns, we investigated their impact by varying two sets of properties: (i) accounting for the effect of PMFs on the initial matter power spectrum and (ii) accounting for their magneto-hydrodynamical effects on the formation of galaxies. By comparing both, we can determine the dominant agent in shaping galaxy evolution.

Methods. We used the magneto-hydrodynamics code RAMSES to generate multiple new zoom-in simulations for eight different host halos of dwarf galaxies across a wide luminosity range of 10^3–$10^6\,L_\odot$. These halos were selected from a ΛCDM cosmological box, tracking their evolution down to redshift $z = 0$. We explored a variety of primordial magnetic field (comoving) strengths of B_λ ranging from 0.05 to 0.50 nG.

Results. We find that magnetic fields in the interstellar medium not only modify star formation processes in dwarf spheroidal galaxies, but these fields also entirely prevent the formation of stars in less compact, ultra-faint galaxies with halo masses and stellar masses below, respectively, $\sim 2.5 \times 10^9$ and $3 \times 10^6\,M_\odot$. At high redshifts, the impact of PMFs on host halos of dwarf galaxies through the modification of the matter power spectrum is more dominant than the influence of magneto-hydrodynamics in shaping their gaseous structure. Through the amplification of small perturbations ranging in mass from 10^7 to $10^9\,M_\odot$ in the ΛCDM+PMFs matter power spectrum, primordial fields expedite the formation of the first dark matter halos, leading to an earlier onset and a higher star formation rate at redshifts of $z > 9$. We investigated the evolution of various energy components and demonstrated that magnetic fields with an initial strength of $B_\lambda \geq 0.05$ nG exhibit a strong growth of magnetic energy, accompanied by a saturation phase that begins soon after the growth phase. These trends persist consistently, regardless of the initial conditions or whether it is the classical ΛCDM model or ΛCDM modified by PMFs. Lastly, we investigated the impact of PMFs on the present-time observable properties of dwarf galaxies, namely: the half light radius, V-band luminosity, mean metallicity, and velocity dispersion profile. We find that PMFs with moderate strengths of $B_\lambda \leq 0.10$ nG show an impressive agreement with the scaling relations of the observed Local Group dwarfs. However, stronger fields lead to larger sizes and higher velocity dispersions.

Key words. magnetohydrodynamics (MHD) – galaxies: dwarf – galaxies: evolution – galaxies: high-redshift – galaxies: magnetic fields – galaxies: star formation

1. Introduction

Observations reveal the pervasive nature of magnetic fields in our Universe, present on all cosmic scales probed so far, ranging from the small scales of planets, stars, and galaxies (Stevenson 2010; Reiners 2012; Beck 2001; Beck & Wielebinski 2013) to galaxy cluster scales (Clarke et al. 2001; Govoni & Feretti 2004; Vogt & Enßlin 2005). For galaxies in particular, magnetic fields play an important role in the process of star formation (Padoan & Nordlund 2011; Zamora-Avilés et al. 2018; Krumholz & Federrath 2019). They have the potential to increase the gas fragmentation (Inoue & Yoshida 2019), slow down the circumgalactic gas flows (van de Voort et al. 2021), suppress the recycling outflows (Grønnow et al. 2018), and shrink the size of galaxies (Martin-Alvarez et al. 2020). The role of magnetic fields in shaping the complex multi-phase interstellar medium is widely recognized (Iffrig & Hennebelle 2017; Körtgen et al. 2019). Observational data from neighboring galaxies indicate that magnetic energy permeates all phases of the interstellar medium and is approximately in equipartition with the thermal and kinetic energy components (Beck 2015a; Lopez-Rodriguez et al. 2023).

Various theories have been proposed to explain the existence of strong galactic fields with a μG amplitude that are coherent on kpc scales and are detected through radio spectropolarimetry in spiral and ultraluminous infrared galaxies (Fletcher et al. 2011; Beck 2015b; Robishaw et al. 2008; McBride & Heiles 2013) and are even present in high-redshift galaxies (Bernet et al. 2008; Mao et al. 2017; Geach et al. 2023). Amongst them, dynamo mechanisms in collapsed objects (Ichiki & Takahashi 2006; Ryu et al. 2008; Naoz & Narayan 2013; Schober et al. 2013; Martin-Alvarez et al. 2022) and magnetized flows in supernovae explosions (Widrow 2002; Hanayama et al. 2005; Safarzadeh 2018) are solely a channel of amplification and require a seed magnetic field. During the process of galaxy formation, the collapse of gas can result in the entanglement of magnetic flux, which may also serve as another means of amplification and lead to galactic fields (Sur et al. 2012). However, this case requires a strong micro-Gauss initial seed, comparable to what has been observed today.

Seed magnetic fields for the galactic dynamo can be generated by specific astrophysical mechanisms, such as the

⋆ Corresponding author; mahsa.sanati@physics.ox.ac.uk

Biermann battery during structure formation (e.g., Kulsrud et al. 1997; Ryu et al. 1998) or reionization (e.g., Subramanian et al. 1994; Gnedin et al. 2000) or the Weibel instability (Sironi et al. 2023; Zhou et al. 2024). Alternatively, cosmic magnetic fields can be remnants from the early Universe, generated in the course of phase transitions (Hogan 1983; Ratra 1992; Ellis et al. 2019) or during the inflationary expansion (Turner & Widrow 1988; Adshead et al. 2016; Domcke et al. 2019; Fujita & Durrer 2019). Inflation, in particular, provides an ideal mechanism for producing large-scale magnetic fields (Ratra 1992; Turner & Widrow 1988). These fields could undergo further amplification through a small-scale chiral dynamo (Joyce & Shaposhnikov 1997; Schober et al. 2022). Such primordial magnetic fields, when generated during this early epoch, would be amplified during the collapse of density perturbations, and directly explain the magnetic fields observed in galaxies (Kandus et al. 2011; Martin-Alvarez et al. 2021).

Observational evidence of non-negligible magnetism even in the intergalactic medium voids sparked interest in this intriguing possibility, initially explored through pioneering works on magnetically broadened secondary emission from blazars (Neronov & Vovk 2010; Taylor et al. 2011; Tavecchio et al. 2011). This was recently expanded upon by more recent studies addressing this question (Archambault & VERITAS Collaboration 2017; Ackermann et al. 2018; Acciari et al. 2023; Aharonian et al. 2023). The presence of magnetic fields in these relatively quiet environments is difficult to explain purely by an astrophysical process in the late Universe (Bertone et al. 2006; Furlanetto & Loeb 2001; Vazza et al. 2017; O'Sullivan et al. 2020; Arámburo-García et al. 2021; Tjemsland et al. 2024) and would perhaps favor a primordial origin. The recent discovery of magnetized filaments between galaxy clusters reinforces this scenario (Govoni et al. 2019; Carretti et al. 2022). For comprehensive reviews of different scenarios for the generation of magnetic fields, we refer to Widrow (2002), Kandus et al. (2011), and Subramanian (2016).

The main interest in magneto-genesis scenarios with a primordial origin stems from their capacity in simultaneously explaining the $\gtrsim 10^{-16}$ G intergalactic magnetic fields as well as their $\sim 10^{-5}$ G galactic counter-parts without imposing a time constraint for rapid amplification and subsequent reorganization into their observed small and large-scale ISM distribution (e.g., Beck 2015a; Borlaff et al. 2023). The existence of such magnetic fields in the pre-recombination plasma may even help to alleviate the Hubble tension (Jedamzik & Pogosian 2020). This result emerges from an increased rate of recombination in the presence of strong primordial magnetic fields (Galli et al. 2022). Before and during the epoch of recombination, these primordial magnetic fields generate density perturbations in addition to those produced by inflation. These perturbations are mapped on the last scattering surface of the cosmic microwave background (CMB) photons, where primordial magnetic fields can imprint a variety of signals. The trace of a stochastic primordial magnetic field on the CMB map could be observed in the excess temperature and polarization anisotropies (Subramanian et al. 2006; Durrer 2007; Widrow et al. 2012; Planck Collaboration XIII 2016). These magnetically produced anisotropies display a strongly non-Gaussian pattern (Caprini et al. 2009; Seshadri & Subramanian 2009; Trivedi et al. 2014). A comprehensive analysis of the CMB constrains the primordial magnetic field to have an upper limit for its amplitude of a few nano-Gauss smoothed over the spatial scale of 1 Mpc. Alternative observational constraints of primordial magnetic fields stem from Big Bang nucleosynthesis (Kernan et al. 1996, which provides the strongest constraints on all length scales), Sunyaev-Zel'dovich statistics (Tashiro et al. 2009), propagation of ultra-high energy cosmic rays (Bray & Scaife 2018; Alves Batista & Saveliev 2019), two-point shear correlation function from gravitational lensing (Pandey & Sethi 2012), and Lyman-α forest clouds (Pandey & Sethi 2013).

Density perturbations produced by primordial magnetic fields influence the formation of first structures and the total matter power spectrum. This impact commences when the ionized matter is decoupling from photons (Trivedi et al. 2012). At this stage, magnetic Alfvén waves can produce additional motions in the nearly homogeneous background (Tsagas & Maartens 2000). These additional density and velocity perturbations in the baryonic matter (Kim et al. 1996; Wasserman 1978a) are gravitationally coupled to dark matter over-densities and consequently modify the number distribution of the first dark matter halos (Varalakshmi & Nigam 2017; Cheera & Nigam 2018). The magnetically-produced perturbations dominate the standard Λ cold dark matter (ΛCDM) power spectrum at large k-modes (Wasserman 1978a; Gopal & Sethi 2003; Shaw & Lewis 2012) and, therefore, they affect the formation of small scale structures. This region of k-space encompasses the low-mass dark matter halos, hosting the smallest galactic systems, namely: dwarf galaxies (see Simon 2019, for a recent review).

Despite their rank as the most abundant type among galaxies, dwarf galaxies are faint and difficult to observe. Therefore, the best studied population of dwarf galaxies have been discovered in our proximity (McConnachie 2012, updated online catalog), and in the nearby Virgo cluster (Binggeli et al. 1985). With the new window opened by the *James Webb* Space Telescope (JWST) to the young Universe, high-redshift dwarf galaxies further expand our observational data (Jeon & Bromm 2019; Gelli et al. 2021; Yajima et al. 2023). The existing observations reveal the scaling of dwarf properties, from brighter systems, to the regime of ultra faint dwarfs. Some scaling relations that characterize the properties of dwarf galaxies are the size-luminosity (e.g., Patel et al. 2018), metallicity-luminosity (Lequeux et al. 1979; Skillman et al. 1989; Garnett 2002; Tremonti et al. 2004), and luminosity-velocity dispersion (e.g., Battaglia et al. 2008; Walker et al. 2009; Fabrizio et al. 2011, 2016). Thus far, cosmological simulations have been relatively successful in reproducing the scaling relations for dwarf spheroidals (Jeon et al. 2017; Macciò et al. 2017; Revaz & Jablonka 2018; Escala et al. 2018; Wheeler et al. 2019; Agertz et al. 2020; Applebaum et al. 2021; Prgomet et al. 2022). However, the assembly of fainter galaxies within dark matter halos is still subject to persistent tensions in a ΛCDM paradigm. The most prominent are the diversity of sizes (Oman et al. 2015; Relatores et al. 2019; Revaz 2023) and diversity of rotation curves (Oman et al. 2015), satellite planes (Pawlowski & Kroupa 2013), and the too-big-to-fail problem (Boylan-Kolchin et al. 2011, 2012). For a recent review on the long-standing tensions between ΛCDM and Local Group observations, we refer to Bullock & Boylan-Kolchin (2017) and Sales et al. (2022).

Modern cosmological simulations have made significant progress in addressing small-scale challenges in the standard model by incorporating more precise treatments of baryonic physics (e.g., Gutcke et al. 2021; Koudmani et al. 2022; Martin-Alvarez et al. 2023; Hopkins et al. 2023). The importance of magnetic fields in shaping galaxies and their interstellar medium has been recognized and studied by a variety of simulations (Martin-Alvarez et al. 2020; Pakmor et al. 2017; Su et al. 2020). However, accounting for additional factors such

as primordial magnetic fields, which are often ignored in models, will provide new insights into existing tensions. Presenting a suite of cosmological simulations, Sanati et al. (2020) showed the impact of primordial magnetic fields on the formation of dwarf galaxies during the Epoch of Reionization. The aim of this manuscript is to expand on that work, by investigating the role played by primordial magnetic fields in the formation of dwarf galaxies and shaping their global properties, conducting a set of cosmological zoom-in simulations that are designed to self-consistently model: (i) the formation and evolution of dwarf galaxies emerging from a magnetically distorted ΛCDM matter power spectrum and (ii) the growth and amplification of uniform primordial magnetic fields.

This paper is organized as follows. Section 2 reviews the role played by primordial magnetic fields in the early history of the Universe and their influence on the ΛCDM matter power spectrum. The numerical framework to generate and evolve our simulations is described in detail in Section 3. The results are presented in Section 4. We first discuss the first stages in the evolution of dwarf galaxies, including the first star-forming gas halos in Section 4.1. Then, in Section 4.2, we present the evolution of different energy components. In Section 4.3, we follow the star formation history and the scaling relations of our simulated dwarf models. Finally, a summary of our main conclusions and a brief discussion is presented in Section 5.

2. Inclusion of primordial magnetic fields in ΛCDM

In Section 1, we present the notion that cosmic magnetic fields may have originated from the inflationary epoch or phase transitions in the early Universe. Such primordial fields with a stochastic nature modify the baryonic clumping factor, thereby affecting the formation of initial structures and the ΛCDM matter power spectrum. This section provides a detailed review of such effects.

2.1. Primordial magnetic field power spectrum

Primordial magneto-genesis scenarios motivated by inflation, conventionally result in a homogeneous, isotropic and Gaussian random initial magnetic field $\boldsymbol{B}(x,t)$ (Wasserman 1978b; Kim et al. 1996; Gopal & Sethi 2003). The two-point correlation function of a non-helical magnetic field $\boldsymbol{B}$ in Fourier space, therefore, can be described by the relation (see e.g., Shaw & Lewis 2012):

$$\langle B_i(\boldsymbol{k})\, B_j^*(\boldsymbol{k}')\rangle = (2\pi)^3\, \delta(\boldsymbol{k}-\boldsymbol{k}')\frac{P_{ij}(k)}{2}P_B(k), \tag{1}$$

where $k = |\boldsymbol{k}|$ is the comoving wave number. The power spectrum of the primordial magnetic field $P_B(k)$ is defined by a simple power law:

$$P_B(k) = A_B\, k^{n_B}, \tag{2}$$

and projected into the Fourier space, orthogonal to k_i, through the transverse projection tensor[1] $P_{ij}(k) = \delta_{ij} - k_i k_j/k^2$. Here n_B is the slope, and A_B the amplitude of the magnetic power spectrum. While inflationary magneto-genesis models favouring a nearly scale invariant spectrum with $n_B \sim -3$, magnetic field generation during electroweak or quantum chromodynamics (QCD) phase transitions feature a positive value for n_B (see e.g., Durrer & Neronov 2013, for primordial magnetogenesis scenarios and resulting spectra).

Commonly, the amplitude of the spectrum is defined as the variance of magnetic field strength at the present time $\boldsymbol{B}_\lambda(x,t_0)$, smoothed at scales of $\lambda = 2\pi/k_\lambda = 1\,\mathrm{Mpc}$, as

$$\langle B_\lambda^2(x,t_0)\rangle = \frac{1}{\pi^2}\int_0^{k_c} \mathrm{d}\boldsymbol{k}\, k^2\, (2\pi)^3\, \delta(\boldsymbol{k}-\boldsymbol{k}')\frac{P_{ij}(k)}{2}P_B(k), \tag{3}$$

where the integral upper limit $k_c = 1\,\mathrm{Mpc}^{-1}$. From Eq. (3) the amplitude A_B is expressed as (Shaw & Lewis 2012)

$$A_B = \frac{(2\pi)^{n_B+5}\, B_\lambda^2}{2\Gamma\left(\frac{n_B+3}{2}\right) k_\lambda^{n_B+3}}. \tag{4}$$

With this definition, n_B and B_λ fully characterize the primordial magnetic fields. They constitute our main free parameters. In the following section, we will describe the incorporation of primordial magnetic fields into the evolution of density perturbations using the linearized Newtonian theory.

2.2. Evolution of density fluctuations

In the ΛCDM framework, all cosmic structures are the result of primordial quantum field fluctuations. In the early Universe, the causal connection between these small over-densities shapes a nearly scale invariant power spectrum $P(k) \propto k^n$, as a function of wave number k, with $n \simeq 1$ (Harrison 1970; Zeldovich 1972; Peebles & Yu 1970; Planck Collaboration XIII 2016).

In the linear Newtonian paradigm, the evolution of initial density perturbations in the baryonic matter $\delta_\mathrm{b}(\boldsymbol{x},t) = \delta\rho_\mathrm{b}(\boldsymbol{x},t)/\rho_\mathrm{b}$ and the collisionless dark matter $\delta_\mathrm{DM}(\boldsymbol{x},t) = \delta\rho_\mathrm{DM}(\boldsymbol{x},t)/\rho_\mathrm{DM}$ is described by the two following coupled equations (see, e.g., Dodelson 2003),

$$\frac{\partial^2\delta_\mathrm{b}}{\partial t^2} + \left[2\,H(t) + \frac{4\rho_\gamma}{3\rho_\mathrm{b}}n_\mathrm{e}\sigma_\mathrm{T}a\right]\frac{\partial\delta_\mathrm{b}}{\partial t} = c_\mathrm{b}^2\nabla^2\delta_\mathrm{b} + 4\pi G\left[\rho_\mathrm{b}\delta_\mathrm{b} + \rho_\mathrm{DM}\delta_\mathrm{DM}\right] \tag{5}$$

and

$$\frac{\partial^2\delta_\mathrm{DM}}{\partial t^2} + 2\,H(t)\frac{\partial\delta_\mathrm{DM}}{\partial t} = 4\pi G\left[\rho_\mathrm{b}\delta_\mathrm{b} + \rho_\mathrm{DM}\delta_\mathrm{DM}\right]. \tag{6}$$

Here, a is the scale factor, $H = \dot{a}/a$ is the Hubble rate, ρ_b and ρ_γ are respectively the baryon and photon mass density, n_e is the electron number density, σ_T is the Thomson cross section for electron-photon scattering, and c_b is the baryon sound speed.

Prior to recombination, due to the high rate of photon-baryon scatterings, radiation and baryonic matter behave as a sole tightly coupled conducting medium, with the magnetic pressure being insignificant compared to the pressure of the photon-baryon fluid. As soon as photons start to free stream the evolution of baryonic perturbations can no longer be adequately described by Eq. (5). It is thus necessary to incorporate compressional and rotational perturbations in this ionized medium. For that the Lorentz force can be formulated using the tangled field,

$$S(\boldsymbol{x},t) = \frac{\boldsymbol{\nabla}\cdot[\boldsymbol{B}\times(\boldsymbol{\nabla}\times\boldsymbol{B})]}{4\pi\rho_\mathrm{b}(t_0)}. \tag{7}$$

We can now solve the magnetohydrodynamics equation describing the growth of total matter density perturbations (see, e.g., Subramanian & Barrow 1998; Sethi & Subramanian 2005),

$$\frac{\partial^2\delta_m}{\partial t^2} + 2\,H(t)\frac{\partial\delta_m}{\partial t} = 4\pi G\rho_m\delta_m + \frac{\rho_\mathrm{b}}{\rho_m}\frac{\boldsymbol{S}(\boldsymbol{x},t)}{a^3}, \tag{8}$$

[1] The importance of the projection tensor lies in the fact that estimating the perpendicularly projection to the line of sight is easier than measuring the tensor field from the observations in large-scale structure.

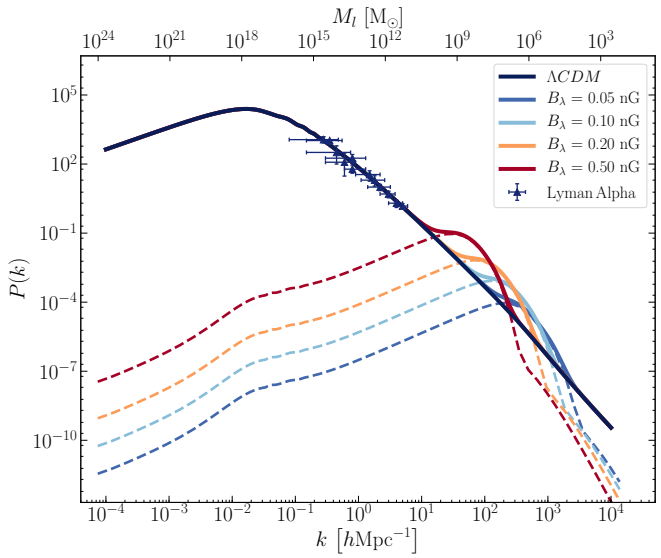

Fig. 1. Impact of primordial magnetic fields on the matter power spectrum varying with increasing field strength. Dashed lines illustrate the distribution of matter induced by primordial magnetic fields, while the solid lines represent the combination of these magnetic-induced matter perturbations and the perturbations produced during inflation. The unperturbed ΛCDM spectrum is shown as the dark blue solid line. The amplitude of the magnetic field is varying from 0.05 to 0.50 nG, while the spectral slope is kept constant at $n_B = -2.9$. The triangles with error bars represent Lyman Alpha data (Tegmark & Zaldarriaga 2002) as the observational constraints on the matter power spectrum at the smallest mass scales.

where $\delta_m = (\rho_{\rm DM}\delta_{\rm DM} + \rho_{\rm b}\delta_{\rm b})/\rho_m$, with $\rho_m = (\rho_{\rm DM} + \rho_{\rm b})$ stands for the summation over both baryonic and dark matter perturbed components. For scales above the Jeans mass, the term representing fluid pressure, $c_{\rm b}^2\nabla^2\delta_{\rm b}$, can be neglected. Following recombination, the damping term in Eq. (5) attributed to the radiative viscousity can also be neglected, as the damping effect caused by the Hubble expansion becomes more important (Jedamzik et al. 1998; Subramanian & Barrow 1998). The growth of perturbations generated by any inhomogeneous[2] magnetic field is then found to be

$$\delta_{m,\rm PMFs}(\boldsymbol{x},t) \simeq \frac{t_{\rm rec}^2\,\boldsymbol{S}(\boldsymbol{x},t_{\rm rec})}{a^3(t_{\rm rec})}\frac{\rho_{\rm b}}{\rho_m}\left[\frac{9}{10}\left(\frac{t}{t_{\rm rec}}\right)^{2/3} + \frac{3}{5}\frac{t_{\rm rec}}{t} - \frac{3}{2}\right], \quad (9)$$

where $t_{\rm rec}$ is the time of recombination epoch. The spatial variation of $\delta_{m,\rm PMFs}(\boldsymbol{x},t)$ in Eq. (9) can be tracked through the magnetic source term $S(\boldsymbol{x},t)$. Therefore, it is expected that the power spectrum of the magnetic field directly affects over-densities on various scales, and ultimately influences the total matter power spectrum.

2.3. Impact on the total matter power spectrum

To understand the effect of primordial magnetic fields on the ΛCDM matter power spectrum, computing the ensemble average of density perturbations is required. In a primordially magnetized early Universe, the total perturbations are the sum of those generated by inflation and the additional perturbations induced by primordial magnetic fields (Kim et al. 1996; Gopal & Sethi 2003). With a Fourier space expression, it leads to

$$P(k,t) = \langle[\delta_m(k,t) + \delta_{m,\rm PMFs}(k,t)]\,[\delta_m^*(k,t) + \delta_{m,\rm PMFs}^*(k,t)]\rangle. \quad (10)$$

Figure 1 showcases $P(k,t)$ at the present epoch. The dark blue line demonstrates the ΛCDM matter power spectrum, resulting from the ensemble average of $[\delta_m(k,t)]^2$. This represents density perturbations obtained from the coupled expressions (in Eqs. 5 and 6) in the absence of primordial magnetic fields. To obtain the matter power spectrum induced by primordial magnetic fields, which is demonstrated by dashed lines, we need the Fourier transform of Eq. (7). Because of the two spatial derivatives in $S(x,t)$, this results in $P_{\rm PMFs}(k,t) = \langle[\delta_{m,\rm PMFs}(k,t)]^2\rangle \propto k^4\,B_\lambda^2 \propto A_B\,k^{2n_B+7}$. At large k modes, perturbations produced by a scale-invariant magnetic spectrum (i.e., $n_B \cong -3$ and $P_{\rm PMFs}(k) \sim k$) dominate the inflationary induced perturbations. However, the magnetic pressure leads to an increase of the Jeans length and denotes the lower limit at which perturbations can collapse. Kim et al. (1996) suggested a formulation for the magnetic Jeans scale which occurs at the transition between growing modes and oscillatory modes,

$$k_{J,B} = \frac{5\pi\rho_{\rm b}\sqrt{G}}{\boldsymbol{B}_\lambda}. \quad (11)$$

By considering the magnetic Jeans length, we arrive at an expression for the shape of dashed lines in Fig. 1, which corresponds to the matter power spectrum induced by primordial magnetic fields, $\langle[\delta_{m,\rm PMFs}(k,t)]^2\rangle$, (Gopal & Sethi 2003),

$$P_{\rm PMFs}(k) \sim A\,k^{2n_B+7} + B\,k_{\rm max}^{2n_B+3}k^4 + C\,k_{\rm max}^{2n_B+1}k^6 + \ldots, \quad (12)$$

Here A, B, and C are coefficients, which (similarly to A_B) only depend on the spectral index. The magnetic counterpart of the Jeans length $k_{\rm max} \cong k_{J,B}$ is regarded as the minimum length scale above which the growth of density perturbations is suppressed. Equation (12) highlights that for $n_B < -1.5$ perturbations on small scales are amplified until they reach $k_{\rm max}$, beyond which they are rapidly quenched. Finally, the solid colored lines in Fig. 1 indicate the total power spectrum obtained from Eq. (10) with the inclusion of both inflationary and magnetically generated perturbations.

To generate the power spectra presented in Fig. 1, we used a modified version of the `CAMB` code (Shaw & Lewis 2012), which incorporates primordial magnetic fields. This version explicitly calculates the non-linear effects of magnetic pressure and the non-negligible viscous damping prior to recombination. Therefore, there is no need for an artificial cutoff wave number, making the power spectrum more accurate compared to analytical studies in the literature. The range of parameters explored in Fig. 1 is carefully selected to affect the power spectrum while still adhering to the constraints presented in Section 1. So, we used a nearly scale-invariant power spectrum with $n_B = -2.9$, and examine a variety of magnetic field amplitudes, $B_\lambda = 0.05$, 0.10, 0.20, 0.50 nG. In the top axis, we show the link between the scales in Fourier space and the corresponding mass scales in real space. For that, we define the mass enclosed within a comoving Lagrangian sphere of radius $r_l \cong 2\pi/k$ at the present epoch, (see e.g., Bullock & Boylan-Kolchin 2017),

$$M_l = \frac{4\pi}{3}r_l^3\rho_m = \frac{\Omega_{\rm m}H_0^2}{2G}r_l^3$$
$$= 1.71\times10^{11}\,{\rm M}_\odot\left(\frac{\Omega_{\rm m}}{0.3}\right)\left(\frac{h}{0.67}\right)^2\left(\frac{r_l}{1\,{\rm Mpc}}\right)^3, \quad (13)$$

[2] The homogeneous solutions are related to fluctuations produced by sources before recombination.

where H_0 is the Hubble constant. With this definition, it becomes evident that the tilt in the matter power spectrum appears in the mass ranges that encompass the dark matter halos of dwarf galaxies. Consequently, we expect that the formation and characteristics of dwarfs could be substantially affected by the presence of primordial magnetic fields.

3. Numerical methods and simulations

We generated all the cosmological simulations studied in this work employing our modified version of the RAMSES code (Teyssier 2002). In addition to the collisionless dark matter and stellar particles, RAMSES employs an adaptive mesh refinement octree grid to solve the evolution of gas. The code models ideal magneto-hydrodynamics (MHD; Fromang et al. 2006; Teyssier et al. 2006), in addition to treating baryonic physics, such as redshift-evolving and uniform UV heating, gas cooling, star formation, and stellar feedback. We provide a brief summary of its essential elements below.

3.1. Numerical setup

Ideal MHD. In its ideal MHD implementation, RAMSES employs a constrained transport (CT) method (Teyssier et al. 2006; Fromang et al. 2006) to solve the equations that govern the evolution of magnetic fields. The induction equation is solved in a conserved integral form on the cell faces. This requires magnetic fields to be stored as six fields on the cell faces. This is unlike all the hydrodynamic quantities in the simulation, namely, densities, velocities, and energy components which are stored at the center of each gas cell. The CT method ensures that the magnetic field has zero divergence up to numerical precision, preventing any unwanted modifications of conserved quantities (Tóth 2000) or the emergence of magneto-hydrodynamical artifacts (Hopkins & Raives 2016).

In the ideal MHD setup, assuming a highly conductive medium, the induction equation is solved with negligible diffusivity but we note that numerical diffusivity is present because finite size of the grid cells. Additionally, the distortion of the primordial field due to the velocity perturbations is only significant at sufficiently small scales and can be disregarded at galactic scales (Wasserman 1978a; Peebles 1980). In the absence of non-ideal magnetic sources such as the Biermann battery, this leads to $\partial\,(a^2\boldsymbol{B}_\lambda)/\partial t = 0$ for the time evolution of the field. As the growth of compressional modes is suppressed before recombination, it solves as $\boldsymbol{B}_\lambda(\boldsymbol{x}, t) = \boldsymbol{B}_\lambda(\boldsymbol{x}, t_{\rm rec})\, a^2(t_{\rm rec})/a^2(t)$, where $\boldsymbol{B}_\lambda(\boldsymbol{x}, t_{\rm rec})$ refers to the value of the magnetic field at recombination ($t = t_{\rm rec}$). In this work, the primordial magnetic field is modeled by an ab-initio $\boldsymbol{B}_\lambda$ that is seeded uniformly and aligned with the z-axis of the computational domain. Mtchedlidze et al. (2023) show that the influence of the initial topology on the final distribution of magnetic fields becomes apparent at the large scale of galaxy clusters and filaments. While for the matter power spectrum, we assume a magnetic energy spectrum with a power-law shape, we use a large-scale magnetic field as the initial B_λ seed in the simulations. This choice of a uniform field is common practice amongst MHD simulations (e.g., Vazza et al. 2014; Pakmor et al. 2017; Martin-Alvarez et al. 2018), but we note that smaller-scale perturbations for such strong initial fields may influence the magnetic field amplification and galaxy formation during the early stages of simulations. Specifically the turbulence-driven growth of magnetic fields on small scales is limited by the spatial resolution of our simulations. Most importantly, the rate of amplification over time increases with finer grid resolution, but also the saturation level might vary (Rieder & Teyssier 2017a; Vazza et al. 2018).

Radiative cooling and heating processes. In addition to primordial gas cooling, we account for metal-line cooling according to the gas metallicity. Above temperatures of 10^4 K, we interpolated the corresponding CLOUDY tables (Ferland et al. 1998). Below 10^4 K, we followed the fine structure metal cooling rates from Rosen & Bregman (1995). We modeled the process of reionization, based on the prediction from Haardt & Madau (1996), using a redshift-dependent UV background that we initialized at $z = 10$. Hydrogen self-shielding against the ionizing radiation was incorporated by suppressing the UV-background heating for gas densities above $n_{\rm H} = 0.01\,{\rm g\,cm^{-3}}$. To account for the pre-enrichment by the Population III stars, we assumed a metallicity floor of [Fe/H] = −5. Above this metallicity, the fine-structure line cooling of atomic carbon and oxygen (Bromm & Loeb 2003), lead to gas fragmentation and the formation of low-mass stars.

Star formation. We modeled the process of star formation by employing a magneto-thermo-turbulent (MTT) star formation prescription, presented in more detail in the hydrodynamical version by Kimm et al. (2017) and Trebitsch et al. (2017) and in its MHD version by Martin-Alvarez et al. (2020). As a brief summary of this star formation model, we note that gas is allowed to transform into stellar particles only in cells that are at the highest level of refinement, where the local combination of magnetic, thermal and turbulent support is overcomed by the gravitational pull (Rasera & Teyssier 2006). The conversion of gas into stars in star forming cells follows the Schmidt law (Schmidt 1959),

$$\dot{\rho}_\star = \epsilon_{\rm ff}\frac{\rho_{\rm gas}}{t_{\rm ff}}. \tag{14}$$

Here, the star-forming gas with a density of $\rho_{\rm gas}$ is converted into stars, with free-fall time $t_{\rm ff}$. In our formulation, the efficiency of this conversion $\epsilon_{\rm ff}$ is not a constant, but rather computed locally based on the gas properties of each region. It was calculated following the multi-scale model of (Padoan & Nordlund 2011) as presented in Federrath & Klessen (2012).

Stellar feedback. Each stellar particle in our simulations corresponds to a single stellar population that is characterized by its own initial mass function (IMF). The IMF is modeled as a probability distribution function following a Kroupa shape (Kroupa 2001) and normalized over the complete range of masses. This allows each stellar particle of mass 294.81 $M_\odot$ to stochastically populate stars within the mass interval of [0.05−50] $M_\odot$ during the initial 50 Myr of its formation. The number of exploding supernovae for each particle is then calculated at each time step based on the lifetimes of stars it contained.

We used the mechanical supernovae feedback prescription of Kimm & Cen (2014), for stellar particles undergoing a supernova event. In this approach, the momentum injected by supernova explosions is determined by the physical characteristics of the gas being swept up, such as its density, $n_{\rm H}$, and metallicity, Z,

$$p_{\rm SN}(E,\, n_{\rm H},\, Z) \approx 3\times10^5\,{\rm km\,s^{-1}}\,{\rm M_\odot}\,E_{51}^{16/17}\,n_{\rm H}^{-2/17}\,f(Z), \tag{15}$$

where the momentum input is decreasing with metallicity as $f(Z) = \max[{\rm Z/Z_\odot}, 0.01]^{-0.14}$. Here E_{51} is the energy in the unit of 10^{51} erg, and $n_{\rm H}$ the hydrogen number density. This method ensures that the feedback from supernovae is accurately modeled at all blast wave stages, from the initial free expansion to the final momentum-conserving snowplow phase. Along with the momentum, energy is deposited into the neighboring cells. The specific

energy of each supernova (SN) has a value $\varepsilon_{\rm SN} = E_{\rm SN}/M_{\rm SN}$, where $E_{\rm SN} = 10^{51}$ erg and $M_{\rm SN} = 10\,{\rm M}_\odot$. Each supernova also returns a fraction of stellar mass back to the ISM. We use $\eta_{\rm SN} = 0.213$ for fraction of $M_{\rm SN}$ returned as gas mass, and $\eta_{\rm metal} = 0.075$ for the newly synthesized metals. This set of values is selected to match the model galaxies in the fiducial setting with the observed global properties of Local Group dwarfs (see Sect. 4.4). Our feedback prescription does not include stellar winds, local radiation from young stars, photo-electric heating, and cosmic rays, all of which, in addition to supernovae feedback, can potentially reduce the final stellar mass of our galaxies.

3.2. Initial conditions

The initial conditions are generated using the `MUSIC` code (Hahn & Abel 2011), and the cosmology of Planck Collaboration XLVII (2016) with $\Omega_\Lambda = 0.685$, $\Omega_{\rm m} = 0.315$, $\Omega_{\rm b} = 0.0486$, and $h = 0.673$. All simulations are started at redshift $z = 200$, ensuring that the rms variance of the initial density field, σ_8, lies between 0.1 and 0.2 (Knebe et al. 2009; Oñorbe et al. 2015). Except for a small subset, all of our simulations are run until a redshift of $z = 0$.

The twelve halos studied in this work are selected from different regions in the dark matter only cosmological box of Revaz & Jablonka (2018). Those regions are identified to form a dark matter halo with a mass typical of spheroidal and ultra-faint dwarf galaxies at redshift $z = 0$. We re-simulate those halos, including the full treatment of baryons described above. Using the zoom-in technique, for each halo we refine a 3D ellipsoid of size about 0.85 cMpc across, positioned in the center of the cubic simulation box with $L_{\rm Box} = 5.11$ cMpc per side. The size of the ellipsoid is determined such that it encompasses all particles that eventually reside within each target halo by redshift $z = 0$ (Oñorbe et al. 2014). In this refined region, we achieve dark matter mass resolution of $m_{\rm DM} \simeq 4 \times 10^3\,{\rm M}_\odot$. We gradually degrade the resolution, from level 10 to 6 of `MUSIC` outside the zoom region[3].

Initially, the domain is discretized with a uniform grid of 1024^3 cells. This resolution is preserved within the zoom region, while the grid is de-refined to level 6 elsewhere. Throughout the course of the simulation, the adaptive refinement criteria come into play to effectively resolve dense and Jeans-unstable regions. When the total dark matter and gas mass within a grid cell exceeds $8\,m_{\rm DM}$, or when the size of the grid cell surpasses 4 local Jeans length, a parent grid cell is split into 8 equal child cells. This process follows the octree structure of `RAMSES`, where the size of cell i is determined by the refinement level of cell l_i according to $\Delta x_i = 1/2^{l_i}\,L_{\rm Box}$. In our simulations, with a maximum refinement level of 20, the initial grid undergoes adaptive refinement to achieve a minimum cell width of approximately 5 pc.

These initial conditions and the configuration of the simulations focus on capturing and resolving the formation of galaxies in halos within the perturbed range of the total matter power spectrum in Fig. 1.

3.3. Set of simulations

We ran nine sets of simulations, which are listed in Table 1. The run which has no magnetic fields and employs a ΛCDM initial configuration is our reference, hereafter denoted as `B00`. In the first series of simulations, a uniform magnetic field is introduced, aligned with the z-axis of the simulation box. The field has an initial comoving strength varied from 0.05 to 0.50 nG, which later evolves self-consistently throughout the simulation. The initial matter power spectrum is set using the ΛCDM paradigm, where no additional perturbation due to primordial magnetic fields is included. Models in this set are denoted by `B05`, `B10`, `B20`, `B50`. In the second series of simulations, in addition to the initial uniform field of comoving strength ranging from 0.05 to 0.50 nG, the effect of primordial fields on the matter power spectrum is taken into account. In these models, denoted as `B05ps`, `B10ps`, `B20ps`, `B50ps`, the initial conditions are generated from a `ΛCDM+PMFs` power spectrum. In each model, the amplitude of the primordial magnetic field is the same as the uniform field in the MHD configuration initiated at redshift $z = 200$, and the spectral index is set to $n_B = -2.9$ to have a scale-invariant magnetic power spectrum.

All the simulations are designed to investigate primordial magnetic fields with strengths allowed by current cosmological constraints (see Section 1). From Fig. 1, it appears that a stronger amplitude than the maximum one used in this work ($B_\lambda = 0.50$ nG) would affect the power spectrum at scales of $k < 10\,h\,{\rm Mpc}^{-1}$. However, such a modification is ruled out by the observations of the Lyman-α forest (Tegmark & Zaldarriaga 2002; Pandey & Sethi 2013). The smallest amplitude employed ($B_\lambda = 0.05$ nG) lies at the threshold where primordial magnetic fields start to affect the ΛCDM power spectrum and potentially exert an influence on structure formation (Shaw & Lewis 2010; Pandey et al. 2015; Sanati et al. 2020).

3.4. Extraction of the observables, luminosity and metallicity

Galactic region. Global galactic properties, such as gas mass and specific energies, are measured inside the galactic region. It is defined using the virial radius of the dark matter halo R_{200} at redshift $z = 0$. The galactic region is the spherical volume centered on the position of the galaxy with radius equal to the comoving evolution of $\sim 1.5\,R_{200}$ ($z = 0$). This method is employed to adaptively increase the size of the studied region as the galaxy and its hosting dark matter halo grow in size. In order to obtain the centre of the galaxy, we tag the system by finding its position at redshift $z \sim 7$. From that point onwards, at each coarse time-step of `RAMSES` we re-compute the position of the galaxy centre. To do this, we simply obtain the new center of mass of the most central ~50 stellar particles in the previous iteration. We use this approach to compute various galaxy properties on-the-fly, with time resolution equivalent to that of the coarse time-stepping of the simulation.

V-band luminosity. The galaxy V-band luminosity (L_V) was obtained by summing the luminosities of all stellar particles located within 1.8 times the halo's half-light radius. Their mass was converted into luminosity using the stellar population synthesis model of Vazdekis et al. (1996) computed with the revised Kroupa (2001) IMF. Where necessary, the luminosities were inter- and extra-polated in age and metallicity using a bivariate spline. We ignored the dust absorption, as its role only becomes critical for intrinsic magnitudes brighter than $M_{\rm AB} \sim -20$ (Ma et al. 2018).

Metallicity. Due to the limited number of stars forming in dwarf galaxies, selecting a representative *mean* [Fe/H] is a non-trivial undertaking. Since the metallicity distribution is sparsely sampled, calculating the mode (peak) of the metallicity

[3] One resolution level l corresponds to $N = (2^l)^3$ particles in the full cosmological box. The particle mass is thus decreased by a factor of eight between two levels.

Table 1. Parameters varying in the simulation runs.

ID	B00	B05	B10	B20	B50	B05ps	B10ps	B20ps	B50ps
B_λ [nG]	0	0.05	0.10	0.20	0.50	0.05	0.10	0.20	0.50
Power spectrum			ΛCDM				ΛCDM+PMFs		

Notes. Columns are as follows: (1) Model ID. (2) Comoving strength of the initial primordial magnetic field. (3) Matter power spectrum used to generate the initial conditions.

Table 2. Global properties of the eight halos simulated in our fiducial hydrodynamical model B00, at redshift $z = 0$.

Halo ID	L_V [10^5 L$_\odot$]	$M_\star$ [10^5 M$_\odot$]	M_{200} [10^9 M$_\odot$]	R_{200} [kpc]	$r_{1/2}$ [kpc]	$\sigma_{\rm LOS}$ [km/s]	[Fe/H] [dex]
h025	9.55	19.67	8.90	65.6	0.57	9.4	−1.95
h070	1.02	2.42	2.16	40.2	0.50	6.0	−2.73
h063	0.58	1.44	2.49	42.2	0.82	4.4	−2.41
h177	0.31	0.78	0.61	26.4	0.45	4.5	−2.42
h111	0.16	0.38	1.25	33.6	0.35	5.0	−2.94
h159	0.24	0.59	0.78	28.7	0.42	4.8	−2.69
h277	0.09	0.21	0.90	30.0	2.00	5.9	−2.65
h190	0.06	0.15	0.57	25.8	0.72	3.8	−3.04

Notes. The first column gives the halo ID following Revaz & Jablonka (2018). L_V is the V-band luminosity and $M_\star$ the stellar mass. M_{200} is the virial mass, i.e., the mass inside the virial radius R_{200}. $\sigma_{\rm LOS}$ is the line-of-sight velocity dispersion and [Fe/H] is the abundance ratio of iron with respect to hydrogen.

distribution function can result in significant uncertainties. In this study, we used the method proposed in Sanati et al. (2023) to determine the mode based on a fitting analytical formula derived from a simple chemical evolution model. The error on [Fe/H] is taken at the maximum of the errors obtained by the different methods, peak, and mode.

Velocity dispersion. The line-of-sight stellar velocity dispersion, $\sigma_{\rm LOS}$, is calculated for seven different lines of sight inside a 1 kpc cylindrical radius. The value quoted for each galaxy represents the mean of these values.

4. Results

Our simulations follow the evolution of six different ultra-faints and two spheroidal dwarf galaxy with final luminosities $\sim 10^3$–10^5 $L_\odot$. Table 2 summarizes the main properties of model galaxies in our fiducial hydrodynamical model B00, at redshift $z = 0$. IDs are those of Revaz & Jablonka (2018, see their Table 1). The seven other columns show the galaxy total V-band luminosity L_V, total stellar mass, $M_\star$, virial mass, M_{200}, virial radius, R_{200}, mean stellar velocity dispersion, $\sigma_{\rm LOS}$, and peak value of the metallicity distribution function, [Fe/H].

4.1. Impact of magnetic fields on gas distribution

Figure 2 shows the density-weighted projection of gas density in the simulated galaxy h070 (see Table 2). The magnetic field strength is increasing from 0.05 nG in the leftmost to 0.50 nG in the rightmost panel. The top and bottom panels correspond to ΛCDM and ΛCDM+PMFs simulation setup, respectively. Snapshots are taken at a redshift of $z = 9$, which corresponds to the intense phase of star formation in dwarf galaxies (Okamoto et al. 2012; Brown et al. 2014; Sacchi et al. 2021; Gallart et al. 2021). The snapshot in model B50ps is shown at redshift $z = 13$, where it stopped due to computational expenses.

We computed the gas mass in each snapshot inside the galactic region (see Section 3.4) which is illustrated by the white circles. The galactic region covers the main halo of the targeted dwarf galaxy and its surrounding in a $1.5 \times R_{\rm vir}$ radius. $M_{\rm gas}$ in the top left of each panel, shows the gas mass within the galactic region averaged over the first 2 Gyr, before the dwarf is completely depleted of gas.

The upper panels correspond to the first set of simulations, where the magnetic fields are initialized as uniform values, as described in Section 3, and the matter power spectrum is that of the classical ΛCDM paradigm. These simulations are designed to explore the contribution of magnetic fields in shaping the internal structure of dwarf galaxies. Here, magnetic fields generate additional pressure support. Along with other hydrodynamical pressures such as the thermal or kinematic, this counteracts the gravitational field and effectively hampers the collapse of gas. It particularly affects the first stages of galaxy formation, i.e., for $z > 6$. The result is that the gas collapse in the first minihalos is delayed by several hundred Myr. The gravitational field in minihalos is therefore less likely to retain the gas when it is heated and pushed out by the UV-radiation at lower redshifts. When $B_\lambda = 0.50$ nG the collapse of gas is completely halted, as shown in the most right panel. This effect leads to a reduction trend in the averaged gas mass with increasing B_λ.

The bottom panels of Fig. 2 represent the second set of simulations, where in addition to varying the strength of the magnetic field seeds, we include their effect on the matter power spectrum. These simulations are designed to explore the net effect of primordial magnetic fields through the altered matter power spectrum on the one hand, and the direct magnetically-produced turbulence and pressure, on the other hand. Here the amplitude of the primordial fields varies from $B_\lambda = 0.05$ to 0.50 nG. The first two columns correspond to models with relatively weaker magnetism. The gas density maps in these two models resemble their counterparts in the first row. Indeed, the impact of weak primordial fields on the matter power spectrum and consequently

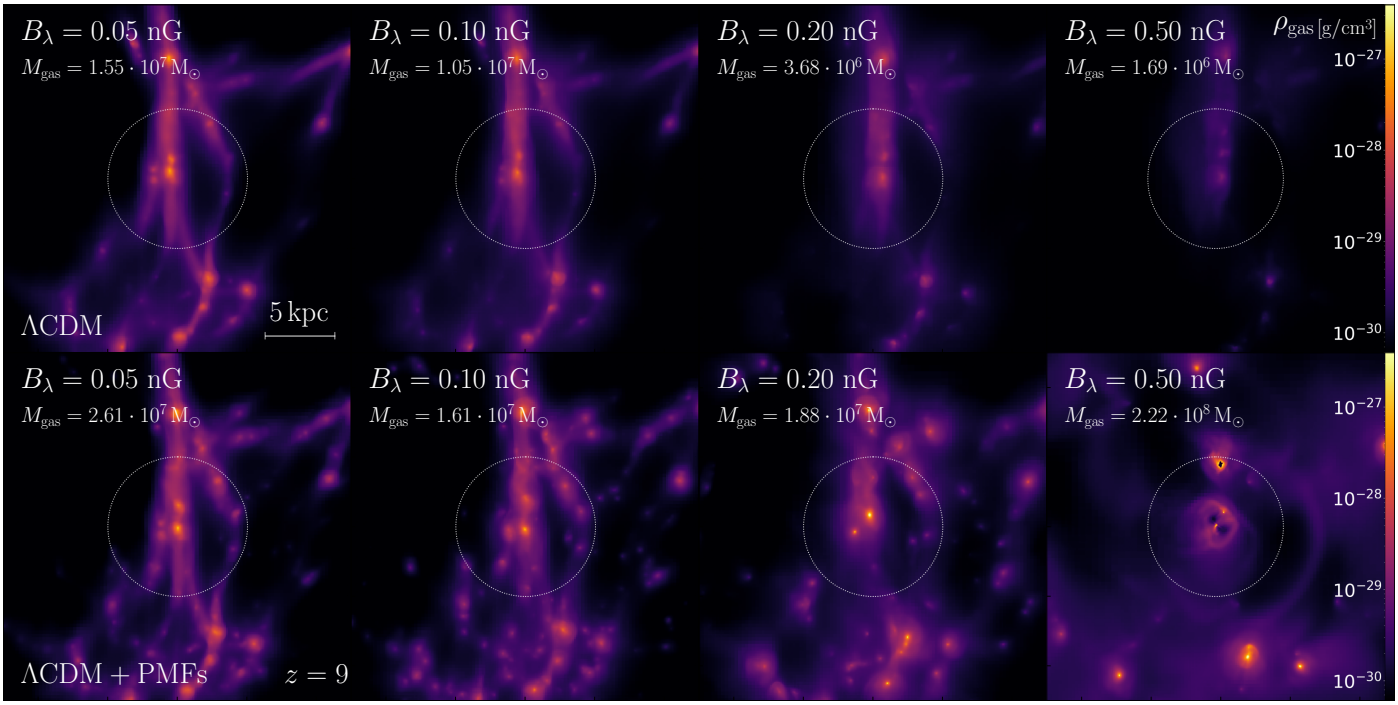

Fig. 2. Gas density projections of model galaxy `h070`. The strength of the magnetic field is increasing from $B_\lambda = 0.05$ nG on the left to $B_\lambda = 0.50$ nG at the rightmost panels. The upper and lower rows represent all the models generated without primordial magnetic fields (ΛCDM), and with primordial magnetic fields (ΛCDM+PMFs) matter power spectrum, respectively. Snapshots are taken at redshift $z = 9$. The white circle shows the galactic region, which is traced in all time steps. The evolution of various galaxy quantities, such as the gas content, is evaluated inside this region with radius ∼1.5 virial radius of the dark matter halo. Panels have physical sides and depth of 256 kpc. The included gas mass represents the average mass of gas in the galactic region over the first 2 Gyr.

the buildup of galaxies is slim (see also Sethi & Subramanian 2005; Sanati et al. 2020; Katz et al. 2021). However, the average gas mass experiences a slight increase, which can be attributed to the additional perturbations induced by primordial magnetic fields in the matter distribution. These perturbations lead to an earlier formation of the first dark matter minihalos and an earlier onset (approximately 100 Myr) of gas collapse, which subsequently continues at a higher rate.

Increasing B_λ introduces considerable reformations in the main halo of the galaxy and the number of its subhalos. Dark matter only simulations of Sanati et al. (2020) shows a strong increase in the maximum of the Gaussian halo mass function, up to a factor of 7, when $B_\lambda = 0.20$ and 0.50 nG, compared to their model without magnetically perturbed initial density fluctuations. For $B_\lambda = 0.20$ nG, Fig. 1 suggests that the additional perturbations generated by primordial magnetic fields mainly affect halos with the Jeans mass $M_l \leq 10^8\,{\rm M}_\odot$. This impact is reflected in Fig. 2, where the number of subhalos in this mass range is noticeably increased. Moreover, $M_{\rm gas}$ inside the galactic region, which contains the main halo of the targeted dwarf and its subhalos, is increased.

When $B_\lambda = 0.50$ nG, from Fig. 1 it appears that the altered matter power spectrum influences the formation of halos with mass $M_l \simeq 10^9\,{\rm M}_\odot$. Therefore, in this model, the main halo of the dwarf galaxy is primarily affected. In the final panel of Fig. 2 it is evident that the gas mass is approximately 100 times greater compared to the counterpart derived from the ΛCDM paradigm depicted in the first row. Here, the strong gravitational potential of the central halo, can merge the satellite subhalos and leads to the formation of a massive dwarf galaxy. In this figure the feature in the center of the galactic region indicates a merger between two halos at high redshifts. The feature at the top-right of the galactic region corresponds to the feedback generated by a supernova explosion.

4.2. The evolution of energy components

In this section, we explore the co-evolution of the key components shaping the energy allocation as a dwarf galaxy evolves over time. The three panels in Fig. 3, respectively from top to bottom, represent the time evolution of the magnetic energy, internal energy and our estimate for the compressional evolution of the magnetic energy. For this plot we use dwarf spheroidal `h070`, but the outcomes are similar for other halos examined in this work (see Table 2). Note that the gas content within the galaxy halo, at different time steps, is subject to the natural mass growth due to accretions, mergers and outflows. Equally, computing the total energy over time is sensitive to the shape and volume of a galaxy. Therefore, for a fair comparison between different energy components, we use specific energies

$$\varepsilon_{{\rm e}_i} = \frac{E_{{\rm e}_i}}{M_{\rm gas}}, \tag{16}$$

as the ratio between the total energy $E_{{\rm e}_i}$ of component ${\rm e}_i$ and the gas mass $M_{\rm gas}$, inside the galactic region (see Section 3.4). The main amplification of the magnetic energy is expected to occur before $z = 2$ (Bernet et al. 2008). During this period, gas kinetic energy is converted into magnetic through magnetic field amplification by a small-scale dynamo, reaching equipartition levels (Groves et al. 2003). After this redshift, magnetism is observed to be in equipartition with other energy components (Wolfe et al. 1992; Basu & Roy 2013; Beck 2015b). For that reason and for clarity, we truncate the time evolution of energies in this plot

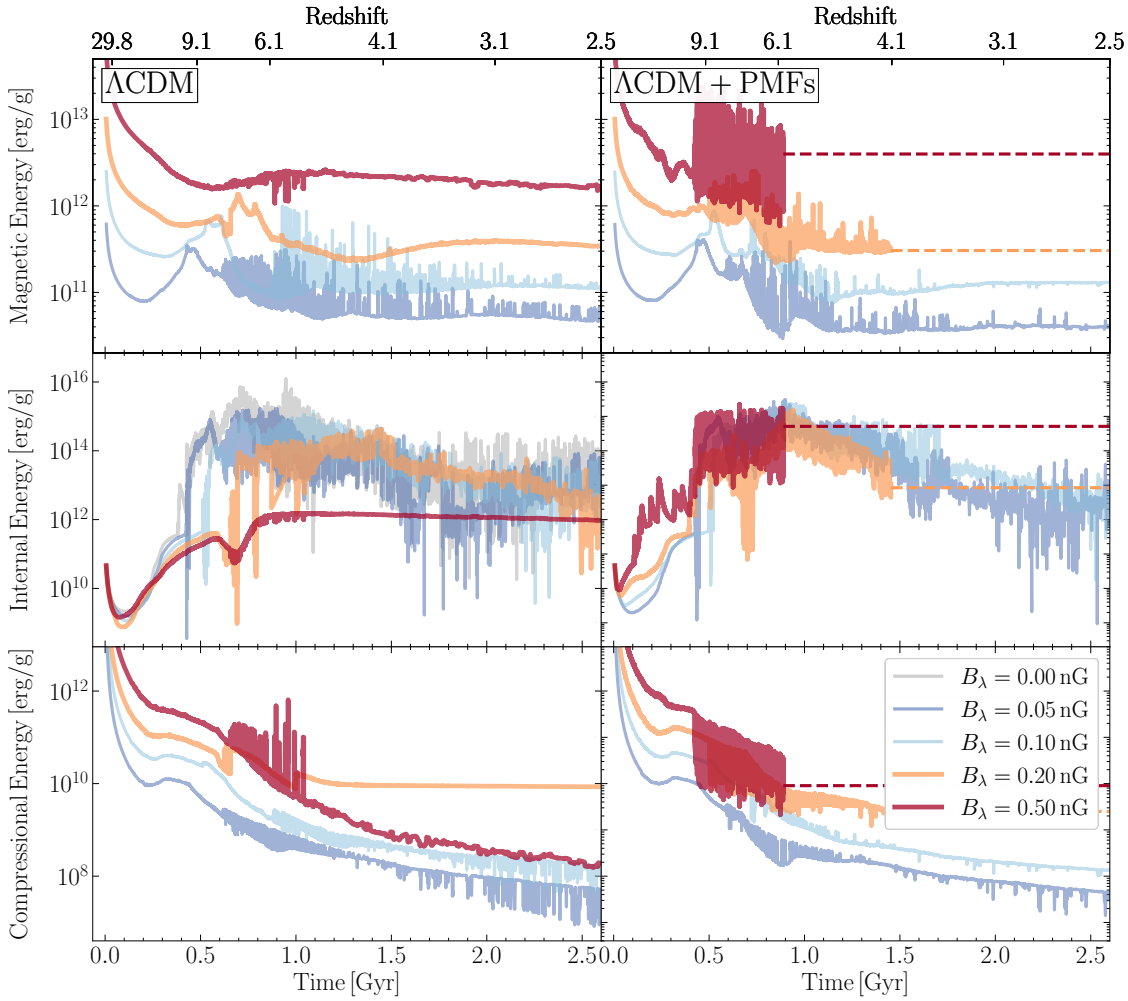

Fig. 3. Comparison of different specific energy components within the galactic region (white circle in Fig. 2) of `h070`. The left and right panels represent all the MHD runs emerging from a standard ΛCDM and ΛCDM+PMFs matter power spectrum, respectively. The upper panels show the time evolution of specific magnetic energy. The ratio of magnetic energy between different models with initial seeds between 0.05 to 0.50 nG increases by a factor smaller than $B_\lambda^2/8\pi$, suggesting energy loss due to magnetic field saturation, including energy dissipation during the collapse. The middle panels show the specific internal energy, which tracks the onset and rate of star formation. The lower panels show the estimate for the compressional part of the magnetic energy from isotropic adiabatic gas collapse. Magnetic energy initially follows the compressional energy as $B_\lambda^2 \propto \rho_{\rm gas}^{4/3}$, until magnetic field amplification causes a deviation in their time evolution.

at 2 Gyr. Each line represents a different model from Table 1, where color codes are the same as in Fig. 1. In the left column, the galaxy simulated using a classical matter power spectrum with the strength of the magnetic field varying from $B_\lambda = 0.05$ to 0.50 nG, showcases `B05`, `B10`, `B20`, and `B50` models. In the right column, the magnetically-induced matter perturbations by primordial fields are also included in the models `B05ps`, `B10ps`, `B20ps`, and `B50ps`. The extrapolation of energy components in models `B20ps`, and `B50ps` which are stopped at redshifts $z \sim 4$ and 6, respectively, due to computational expenses is shown by dashed lines.

Magnetic energy. The topmost panels show the specific magnetic energy $\varepsilon_{\rm mag}$ as it evolves over time. The time evolution of the magnetic field is described by the induction equation:

$$\frac{1}{a}\frac{\partial(a^2\boldsymbol{B}_\lambda)}{\partial t} = \boldsymbol{\nabla}\times\left[\boldsymbol{v}\times(a^2\boldsymbol{B}_\lambda) - \frac{1}{a}\eta\,\boldsymbol{\nabla}\times(a^2\boldsymbol{B}_\lambda)\right]. \quad (17)$$

In the absence of resistivity ($\eta = 0$), peculiar velocities ($\boldsymbol{v} = 0$) and non-ideal magnetic sources such as Biermann battery (Biermann 1950), this leads to $\partial(a^2\boldsymbol{B}_\lambda)/\partial t = 0$. Before density fluctuations start collapsing into structures, both magnetic fields and gas density are decreasing with the expansion of the Universe as $1/a^2$ and $1/a^3$, respectively, shaping the relation $B_\lambda^2 \propto \rho_{\rm gas}^{4/3}$. The magnetic flux freezing to the plasma is imprinted in the early decaying of the specific magnetic energy at high redshifts, as shown in the topmost panels of Fig. 3. After this phase, magnetic energy begins to grow due to the compression of the fields as the first structures start to collapse.

As expected, models with stronger initial seeds ($B_\lambda = 0.20$ and 0.50 nG) reach higher magnetic energy values during their evolution. This pattern is evident in both the unperturbed ΛCDM set of simulations and the magnetically-perturbed set, as depicted in the left and right columns, respectively. Models in the `ΛCDM` setup, show the impact of magnetic fields acting against the gravitational potential. This causes a delay in the collapse of halos and the growth of magnetic energy. The severeness of this delay depends on the strength of the magnetic initial seed. Similar simulations of Martin-Alvarez et al. (2021) obtain a

comparable value of $\varepsilon_{\rm mag} \sim 10^{11-12}$ erg/g at high redshifts before the magnetic energy reaches saturation.

It is interesting that the energy ratios in each set of runs do not increase by a factor of $B_\lambda^2/8\pi$. For instance, when we compare the `B0.05` and `B0.10` models, one might anticipate a 2^2 increase in energy due to a stronger initial magnetic seed. However, a smaller energy increase of ∼2.7 suggests energy loss due to magnetic field saturation, with some energy dissipation even occurring during the collapse phase. The saturation of magnetic energy becomes more pronounced in stronger models and can occur within relatively short time intervals, such as a few hundred Myr. This behaviour is followed in both sets of simulations presented in the left and right panels. In models featuring weaker magnetization ($B_\lambda = 0.05$ and 0.10 nG), it takes a longer period for the magnetic energy to reach saturation.

Internal energy. The middle panels show the specific internal energy $\varepsilon_{\rm int}$, as a function of time. In the ΛCDM setup, the internal energy gradually decreases as the value of B_λ increases from 0.05 to 0.50 nG. This decline can be attributed to the supplementary pressure support exerted by magnetic fields, which also opposes the collapse of gas clouds (see the discussion in Section 4.1) and hinders star formation. Given that the internal energy closely tracks the heating generated by the stellar feedback, raising the magnetic field strength leads to a decrease in the number of peaks and valleys, as well as the amplitude of $\varepsilon_{\rm int}$.

This reduction in internal energy is particularly pronounced during the early stages of galaxy formation, specially at redshifts $z > 6$, distinguishing the stronger models `B0.20` and `B0.50` from the weaker models `B0.05` and `B0.10`. In the extreme case of `B0.50`, the star formation is dramatically suppressed and a limited increase of $\varepsilon_{\rm int}$ is observed. Another notable characteristic evident here is the delay in the growth of internal energy when the magnetic field strength is significant, particularly $B_\lambda = 0.20$ and 0.50 nG. The evolution of internal energy closely corresponds to changes in density and temperature and consequently reflects the collapse of gas clouds. Therefore, the delay caused by strong magnetic fields in the formation of minihalos impacts the timing at which $\varepsilon_{\rm int}$ begins to accumulate from its initial value.

In the ΛCDM+PMFs setup, a distinct trend is evident in the right panel compared to the left panel, showcasing the influence of primordial fields. Here, a higher variability is evident in the internal energy, characterized by numerous peaks and valleys, specially in stronger models. This pattern, visible across all strengths of magnetic field, implies a more dynamic star formation history. In these models, the formation of more massive minihalos accelerates the pace of collapse, star formation and consequently influences the rate at which internal energy is growing. Additionally, primordial magnetic fields expedite the onset of minihalo formation. As a result, the collapse of gas clouds is accelerated, leading to the onset of internal energy accumulation within timescales as short as several tens of Myr, specifically when $B_\lambda = 0.50$ nG.

Compressional energy. The bottom panels show the evolution of the specific compressional energy $\varepsilon_{\rm comp}$ versus time. This term is obtained from an isotropic adiabatic approximation of the gas collapse. During the early stages of galaxy formation, the magnetic energy density scales with the gas density as $\propto\rho_{\rm gas}^{4/3}$ (see e.g., Rieder & Teyssier 2017b; Martin-Alvarez et al. 2018). Thus $E_{\rm comp}(t_0) = E_{\rm mag}(t_0) \propto \rho_{\rm gas}^{4/3}(t_0) \times {\rm volume}(t_0)$. In the absence of amplification or decaying processes, this approximation dictates the evolution of the frozen-in magnetic field lines, which closely follow the collapse of cosmic structures, indicating $E_{\rm comp}(t) \propto \rho_{\rm gas}^{4/3}(t) \times {\rm volume}(t)$. To extract this term in each time step of the simulation, we use:

$$E_{\rm comp,cell}(t) = \frac{dx_{\rm cell}^3}{\frac{4}{3}\pi r_{\rm gal}^3(t_0)} \times \langle E_{\rm mag,gal}(t_0)\rangle \times \left(\frac{\rho_{\rm gas,cell}(t)}{\langle\rho_{\rm gas,gal}(t_0)\rangle}\right)^{4/3}, \tag{18}$$

where the compressional energy in each cell of size $dx_{\rm cell}$ and at each time step, t, denoted as $E_{\rm comp,cell}(t)$, is directly proportional to the gas density $\rho_{\rm gas,cell}(t)$ within that particular cell. Then, $\langle E_{\rm mag,gal}(t_0)\rangle$ stands for the average of magnetic energy within the galactic region of radius, $r_{\rm gal}$, at a time, t_0, when it is at its minimum state. This corresponds to the turnaround point, marking the moment when the initial perturbations transition from expansion to collapse. At this moment, when the magnetic energy reaches its lowest value, baryonic matter accumulates and the first stars begin to form within the emerging galaxy. Eventually, the total compressional term is derived by summing over all cells within the galactic region. It is then divided by the total gas mass in this region to obtain the specific energy. By comparing the evolution of magnetic energy and compressional energy, we can investigate the nature of magnetic field amplification. In case of dynamo amplification, it is anticipated that magnetic energy undergoes exponential growth, and the ratio of magnetic energy to compressional energy significantly exceeds 1.

Figure 4 presents the ratio between $E_{\rm mag}$ and $E_{\rm comp}$ as a function of time. As described, the compressional term demonstrates the expected buildup of magnetic fields, when exclusively frozen in the collapse of matter into dark matter halos. The deviation of $E_{\rm mag}$ from $E_{\rm comp}$, apparent in all models, indicates the amplification of magnetic fields through different mechanisms that occur alongside adiabatic magnetic compression. These mechanisms include the activity of a dynamo within collapsing gas clouds. In both upper and lower panels, the ratio initially follows the same curve in all models, as magnetic energy evolves with the expansion of the Universe as $B_\lambda \propto a^{-2}$, until the density perturbations start to collapse. Once the galaxy reaches the turnaround point from expansion to collapse in each model, the ratio takes different paths. Increasing the magnetic field strength results in a slower amplification rate. This is due to a considerably higher $B_\lambda(t_0)$ and B_λ in the galaxy. Thus it takes significantly longer time for the stronger models to reach a similar amplification rate as the weaker ones. The upper and lower panel showcase the same result in ΛCDM and ΛCDM+PMFs setting.

It is worth noting that this amplification can also be attributed to the influence of powerful supernova feedback events. In this scenario, the supernova shock evacuates the surroundings of the exploding star from gas, thus reducing the $E_{\rm comp}$. Simultaneously, the supernova winds push the magnetic fields outwards, while keeping them in the galactic region. Therefore the $E_{\rm mag}/E_{\rm comp}$ ratio is increasing with time.

In order to unravel the source of separation between the compressional and magnetic energy terms, we re-simulate `h070` in model `B05` and `B20`, deactivating the supernovae feedback. The comparison is shown in the upper panel of Fig. 4. The green and yellow dotted lines represent the simulations in which the supernovae feedback is set to zero. The more rapid increase in magnetic energy compared to compressional energy remains evident in simulations without feedback. This indicates that the amplification of magnetic fields is not solely attributed to the supernova explosion process. It further strengthens the notion that magnetic fields initiated with even a week seed, e.g., $B_\lambda = 0.05$ nG can undergo dynamo amplification as the galaxy evolves through

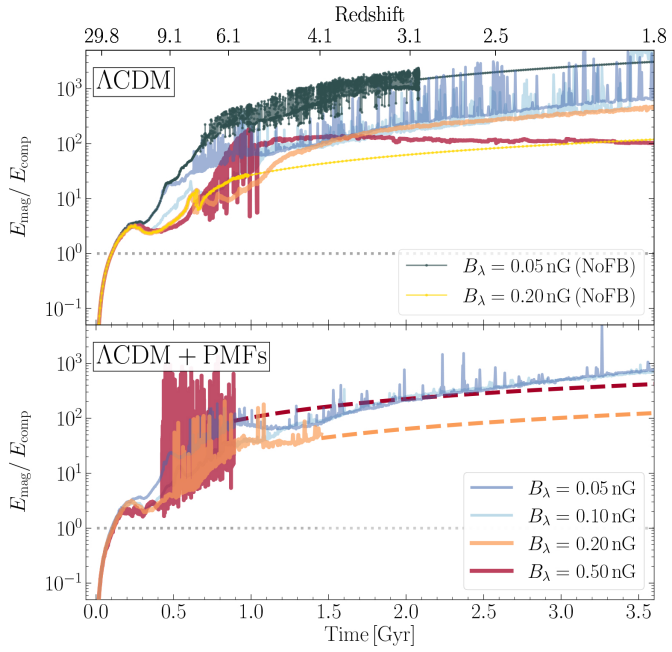

Fig. 4. Time evolution of the ratio of magnetic energy to compression energy in the galactic region (white circle in Fig. 2) for all the simulations during the first 3.5 Gyr. The upper and lower panels corresponds to all the models in ΛCDM and ΛCDM+PMFs settings, respectively. The green and yellow dotted lines in the top panel represent `B0.05` and `B0.20` models re-simulated without supernovae feedback. The more rapid increase in E_{mag} compared to E_{comp} demonstrates the amplification of magnetic fields, even with a week seed (e.g., $B_\lambda = 0.05$ nG), through gas accretion, halo collapse and mergers. This amplification occurs in models with the fiducial value of supernovae feedback $E_{SN} = 10^{51}$ erg and with zero feedback.

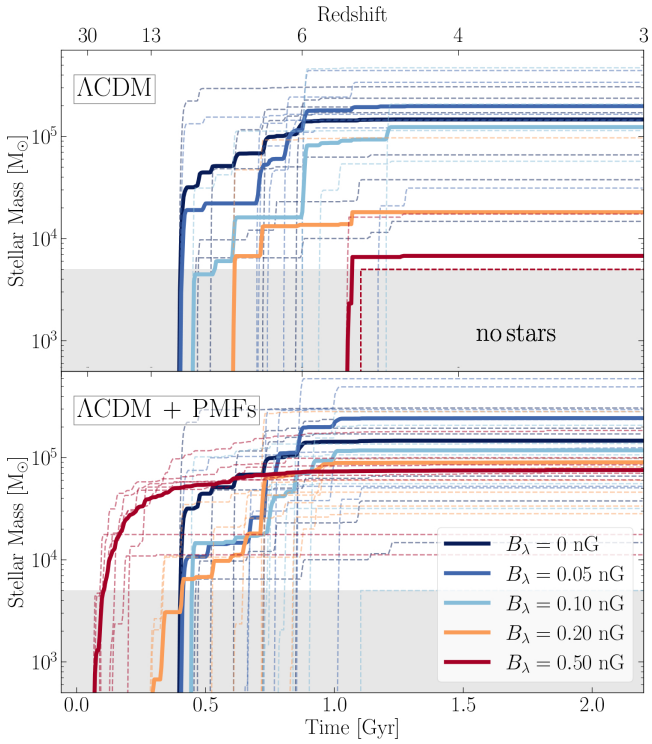

Fig. 5. Cumulative stellar mass during the first 2 Gyr. Each dashed line represents the stellar mass of each model galaxy simulated in a magnetic field model with strength varying from $B_\lambda = 0.05$ to 0.50 nG, compared with the model without magnetic field. Each solid line represents the mean stellar mass of all galaxies simulated in each model. The upper and lower panels correspond to all the models in ΛCDM and ΛCDM+PMFs settings, respectively. Top: Magnetic fields delay the formation of first stars. In low-mass halos of ultra-faint dwarf galaxies, $B_\lambda = 0.50$ nG completely prevents the star formation. In order to include halos which do not form any stars in the plot, their stellar masses are shown at $4 \times 10^3\ M_\odot$. Bottom: The influence of primordial magnetic fields on the matter power spectrum accelerates the formation of the first dark matter halos, leading to an earlier onset of star formation but an overall reduction in the final stellar mass.

gas accretion, halo collapse, and mergers. The higher ratio of E_{mag}/E_{comp} in models without supernovae feedback is because magnetic field back reactions from supernovae explosions slow down the growth of magnetic energy in models with feedback.

4.3. Impact of magnetic fields on star formation

In this section, we present the influence of primordial magnetic fields on the star formation history and final stellar mass of dwarf galaxies. From each zoom-in simulation, we first identify the halo corresponding to the reference halo in the fiducial model. Subsequently, using the position and particle IDs, we extract the correspondent halo in other models. The physical quantities of each galaxy such as the stellar mass are computed inside the virial radius R_{200} of the extracted halo.

Figure 5 displays the cumulative mass of stars forming within the initial 2 Gyr. In each magnetic field model, the line represents the average value of stellar mass measured for all galaxies simulated using the same magnetic field strength. In the fiducial model `B00`, shown in dark blue, star formation is quenched in the simulated galaxies before 1 Gyr at the latest.

In the first set of simulations, the delay induced in the onset of star formation in the MHD configuration can be seen in the top panel of Fig. 5 across all amplitudes of magnetic field examined. This effect is specifically evident in the first Gyr. Following the delay in the birth of first stars, it is difficult for galaxies to catch up with the cumulative star formation in the fiducial model, when the gas is heated by the background UV-radiation. This delay becomes more apparent in models with strong magnetic fields, $B_\lambda = 0.20$ and 0.50 nG, which have a more substantial influence on the gas distribution. In weaker models, $B_\lambda = 0.05$ and 0.10 nG, this delay results in a shortened star formation history of less than 500 Myr, particularly pronounced in ultra-faint dwarf galaxies with a small gas mass. The rate of star formation and the final stellar mass are consistently decreasing as the strength of the magnetic field increases.

The bottom panel of Fig. 5 shows models which include magnetic fields through the altered matter power spectrum ΛCDM+PMFs. One striking outcome of these models is an expedited onset of star formation. This stems from the influence of primordial fields in speeding up the formation of first dark matter halos and their subsequent gas accretion. This effect persists across all amplitudes of magnetic fields examined, further confirming the results obtained in Sanati et al. (2020), for different amplitudes and spectral indices of primordial magnetic fields. However, it is more moderate in models with a weak primordial field. From Fig. 1 it can be seen that the region affected by weakly perturbed models (`B0.05ps` and `B0.10ps`) encompasses halos with a Jeans mass of approximately 10^5–$10^7\ M_\odot$. Consequently, the weakly perturbed models exhibit a slight increase in the abundance of small minihalos within this mass range. However, the gas content in most of these minihalos is insufficient

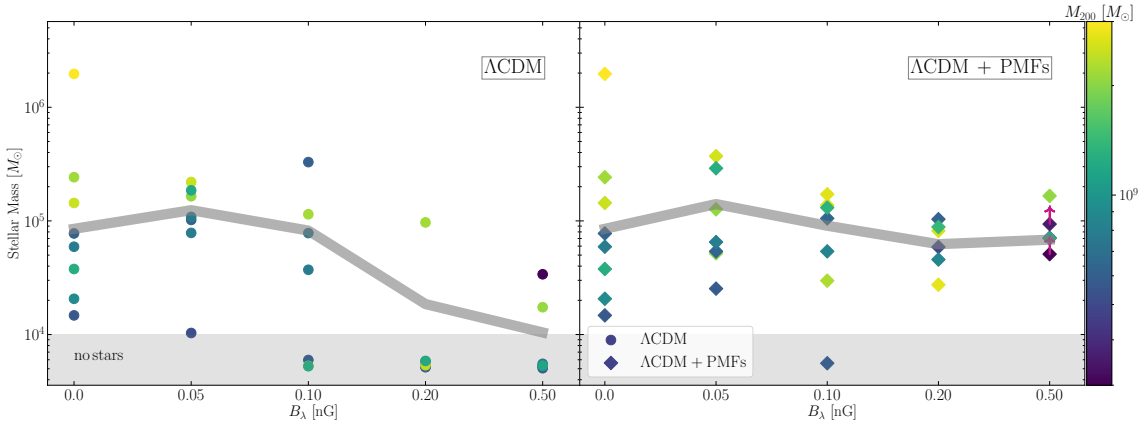

Fig. 6. Stellar mass of each galaxy at redshift $z = 0$ for varying primordial magnetic field strength, color-coded by the virial mass of the dark matter halo. In the left panel, each circle represents one galaxy simulated in the MHD suite (ΛCDM model). In the right panel, galaxies shown as empty diamonds (ΛCDM+PMFs model) consider both magneto-hydrodynamics and the contribution of primordial fields to the matter power spectrum. The stellar mass of halos which do not form any stars is shown at $M_\star < 10^4\ M_\odot$ instead of $0\ M_\odot$. Halos that do not reach redshift $z = 0$, due to extensive CPU-hours required, are identified by marking them with an upward arrow.

to form stars. In these models, the accelerated build up of the galaxies is therefore a secondary effect of primordial magnetic fields when considering stellar masses. Their dominant effect is further counteracting pressure in the ISM.

Increasing the amplitude of primordial magnetic fields affects the matter power spectrum at higher halo masses, as shown in Fig. 1. When $B_\lambda = 0.20$ nG, the abundance of sub-halos with a Jeans mass of approximately 10^8 $M_\odot$ increases. The gas collapse in these halos is able to satisfy the MTT prescription for the formation of stellar particles. The star formation rate, specially during the first 500 Myr, is therefore considerably boosted in this model. Similarly, when $B_\lambda = 0.50$ nG, the main halo of each dwarf galaxy grows in mass. Unlike the effect of the lower amplitudes of B_λ, for these two models, the impact of primordial magnetic fields in accelerating galaxy evolution outweighs their contribution to the overall pressure support and ISM physics. Figure 5 shows that in these two strongly perturbed models star formation is initiated earlier and at higher redshifts compared to the fiducial `B00` model. This implies that primordial magnetic fields can be a potential mechanism to explain the efficient and rapid star formation observed in galaxies at $z \sim 8.5$–14.5 in the CEERS survey (e.g., Finkelstein et al. 2024; Asada et al. 2024).

To quantitatively demonstrate the correlation between star formation and magnetic field strength, Fig. 6 presents the final stellar mass of dwarf galaxies as a function of B_λ. In the left panel, each circle is representative for one galaxy at redshift $z = 0$, color-coded by the virial mass of its dark matter halo. The gray line represents the average stellar mass for all simulated galaxies as a function of magnetic field strength. For both ultra-faints and dwarf spheroidal, the final stellar mass remains largely unaffected in the weak models with $B_\lambda = 0.05$ nG. However, comparing the dwarf spheroidal to ultra faint dwarf galaxies in stronger magnetic field models shows that the low-mass gas content of ultra faints is very sensitive to any perturbations, namely, the impact of magnetic fields. Although the merging history and the star formation history in each ultra-faint galaxy is different, the average trend shows a steady decrease in the final stellar mass.

In the `B0.20` model, only the dwarf spheroidal galaxy within our sample has a non-zero final stellar mass, while the collapse of minihalos and star formation in all of the simulated ultra-faint dwarfs is completely hindered by a magnetic field with a strength of $B_\lambda = 0.20$ nG. For illustrating these halos in Fig. 6, their zero stellar mass is replaced by random values between 5 and 6×10^3 $M_\odot$, and marked with the "no stars" label. A stronger magnetic field with a strength of $B_\lambda = 0.50$ nG prevents the formation of stellar particles with our MTT star formation model in all the ultra-faint dwarf galaxies. Here, the most massive dwarf spheroidal in our sample, `h025`, is used to obtain a threshold for the mass of dwarf galaxies where the impact of magnetic fields become more important in their evolution. Due to computational constraints, simulations for this galaxy are limited to the fiducial model `B0.00` and the extreme MHD model `B0.50`. By comparing this more massive dwarf with lower mass ultra-fain galaxies, it appears that magnetic fields severely quench the star formation in dwarf galaxies with halo mass and stellar mass below $M_{200} \sim 2.5 \times 10^9\ M_\odot$ and $M_\star \sim 3 \times 10^6\ M_\odot$, respectively.

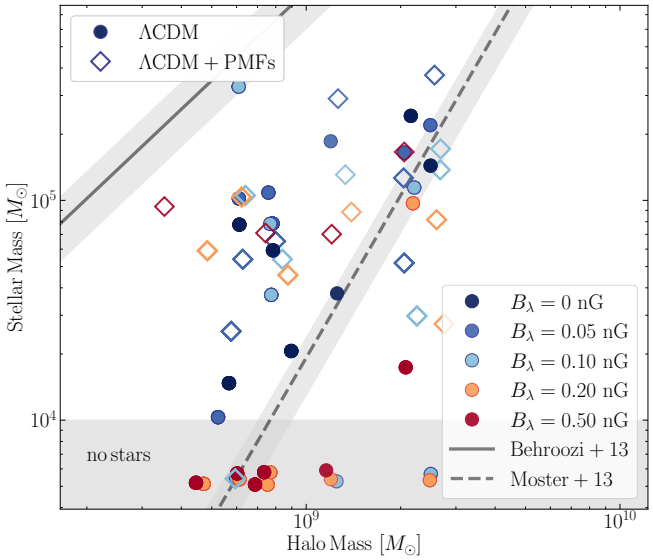

Fig. 7. Relation between galaxy stellar mass and dark matter halo mass for each simulated dwarf galaxy at redshift $z = 0$. For comparison, the extrapolated abundance matching models of Behroozi et al. (2013) and Moster et al. (2013) are shown in solid and dashed lines, respectively. In order to include halos which do not form any stars in the plot, their stellar masses are shown at $M_\star \sim 10^3\ M_\odot$.

The right panel of Fig. 6 shows models which include the impact of primordial magnetic fields on the matter power spectrum (ΛCDM+PMFs) in the MHD setup. Notwithstanding the modifications occurring in the internal structure of dwarf galaxies at high redshifts, the impact of magnetic fields in the ISM remains a vital factor in their evolution throughout the star-forming phase. The result of this dual effect on the final stellar mass of model galaxies is displayed as colored diamonds. In strongly perturbed models, `B20ps` and `B50ps`, despite an increased number of minihalos with a larger gas content, the persistent effect of additional magnetic energy in the ISM counteracting gravitational collapse throughout the entire star formation period leads to a lower stellar mass compared to the fiducial `B00` model at redshift $z = 0$. The noteworthy observation here is that the final stellar mass in halos emerging from the second set of simulations (ΛCDM+PMFs) surpasses that of their counterparts in the first set (ΛCDM). Therefore, for dwarf galaxies with luminosity $L_V < 10^5\,L_\odot$, solely incorporating magnetic fields in numerical simulations while disregarding the influence of primordial fields on their host dark matter halos may result in miscalculation of the impact of primordial magnetic fields in reducing the star formation rate, leading to an overestimation for stronger magnetic field strengths.

4.4. Impact of magnetic fields on scaling relations

In this section, we explore the impact of primordial magnetic fields on the global properties of dwarf galaxies. Namely, the V-band stellar luminosity, stellar mass, virial mass, line-of-sight velocity dispersion, half-light radius, and stellar metallicity. The method for calculating each quantity is described in Section 3.4.

4.4.1. Stellar mass-to-halo mass

Figure 7 shows the relation between galaxy stellar mass and dark matter halo mass for each simulated dwarf galaxy at redshift $z = 0$. The results from the abundance matching models of Behroozi et al. (2013) and Moster et al. (2013) are represented by solid and dashed lines, respectively. Both models have their halo masses extrapolated to $10^8\,M_\odot$ to encompass the mass range of the simulated ultra-faint dwarf galaxies. In the fiducial model `B00`, the resulting stellar masses range from approximately 10^4 to $2.5 \times 10^5\,M_\odot$. All galaxies in this model lie well within the expected values for the final halo mass, which spans from 8×10^8 to $2.5 \times 10^9\,M_\odot$. Note that the stellar masses of these galaxies are lower than that those of the galaxies simulated in Revaz & Jablonka (2018) and Sanati et al. (2020), despite having the same halo mass. This is due to the star formation and stellar feedback schemes varying in different hydrodynamical codes.

Colored circles show halos in the first set of simulations, originating from a ΛCDM paradigm. Magnetism of low strength ($B_\lambda = 0.05$ and 0.10 nG) does not dramatically influence their location in the $M_\star - M_{200}$ relation compared to the fiducial model. Nonetheless, the inverse scaling of the stellar mass with the strength of the field, observed in Section 4.3, persists in this relation as well. For a given halo mass, the final stellar mass decreases with increasing B_λ. Low-mass halos which do not form stars in the strong magnetic field model, where $B_\lambda = 0.20$ and 0.50 nG, are labeled with no stars. To include these halos in the plot, their zero stellar mass is substituted with a random value of $5{-}6 \times 10^3\,M_\odot$.

Colored empty diamonds depict halos in the second set of simulations, emerging from a modified ΛCDM paradigm (ΛCDM+PMFs). The global properties of galaxies undergo only minor changes in the weakly perturbed models. When $B_\lambda = 0.05$ and 0.10 nG, all halos closely resemble their counterparts in the fiducial model. However, in the strongly perturbed models, the final stellar mass recurrently reveals that the influence of primordial magnetic fields on the initial phases of galaxy formation, primarily through modifications to the matter power spectrum, outweighs its subsequent effects in the ISM. Galaxies which do not form stars in the `B0.20` and `B0.50` model, evolve into bright dwarfs with average $M_\star = 6$ and $7 \times 10^4\,M_\odot$ in the `B0.20ps` and `B0.50ps` models, respectively. Since the abundance matching relation is not well constrained in the regime of ultra-faint dwarf galaxies, none of the models is ruled out based on this comparison. It is indeed likely that the same halo mass supports orders of magnitude differences in stellar mass, owing to various environmental effects and unique history of each dwarf galaxy (see i.e., Revaz & Jablonka 2018). This may lead to a considerable scatter in the low-mass regime.

4.4.2. Luminosity-velocity dispersion

Figure 8 shows the V-band luminosity, L_V, versus the line-of-sight velocity dispersion, $\sigma_{\rm LOS}$, for each simulated galaxy at redshift $z = 0$. The comparison to the observational data is obtained from the regularly updated Local Group and Nearby Dwarf Galaxies database of McConnachie (2012), represented by gray squares in the figures.

In the first set of simulations (ΛCDM), represented by colored circles, higher values of B_λ result in a reduced final stellar mass for a given halo mass. Therefore, increasing the strength of magnetic fields, causes the systems to become noticeably fainter than their corresponding analogues in the fiducial model, or even completely stops the star formation. Additionally, magnetic fields impact the line-of-sight velocity dispersion in each halo. In galaxies where magnetic fields of strength $B_\lambda = 0.05$ nG lead to less concentrated star formation and an increased half light radius (see Sect. 4.4.3), there is an associated increase of the velocity dispersion.

In the second set of simulations (ΛCDM+PMFs), represented by colored empty diamonds, incorporating primordial magnetic fields through the matter power spectrum, both the luminosity and the stellar velocity dispersion of the simulated galaxies are modified. Particularly, in the strongly perturbed models, `B20ps` and `B50ps`, despite lower luminosities, the line-of-sight velocity dispersion of each halo is notably larger than in the fiducial model. In these models, due to the impact of primordial magnetic fields on the evolution of dark matter substructures, stars in the main halo of each galaxy migrate from numerous minihalos. In addition, because of greater number of minihalos forming in these models, there is increased frequency of mergers between minihalos. This results in the observed differences in the dynamics of the simulated galaxies.

4.4.3. Size-luminosity relation

Figure 9 displays the half-light radius $r_{1/2}$ of the model dwarf galaxies as a function of their V-band luminosity at redshift $z = 0$. The Local Group dwarfs compiled from McConnachie (2012) are represented by gray squares with error bars. The galaxies simulated in the fiducial model cover a wide range in luminosity

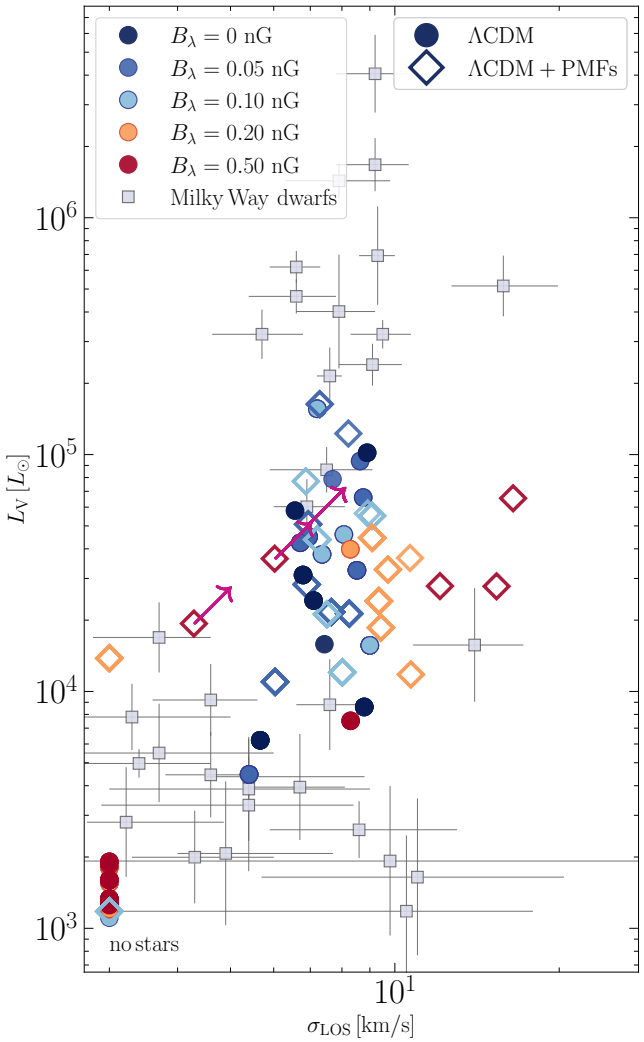

Fig. 8. V-band luminosity as a function of line-of-sight velocity dispersion in each model galaxy is compared to the observational data of Milky Way satellites in gray squares. In the ΛCDM setting, increasing the magnetic field strength results in fainter systems (illustrated by colored circles) and can even completely prevent star formation in ultra-faint dwarf galaxies. In order to include halos which do not form any stars in the plot, their luminosities are represented at $L_V \sim 10^3\,L_\odot$. In the ΛCDM+PMFs setting, despite lower luminosities, velocity dispersion of galaxies (illustrated by colored empty diamonds) increases due to a higher frequency of mergers.

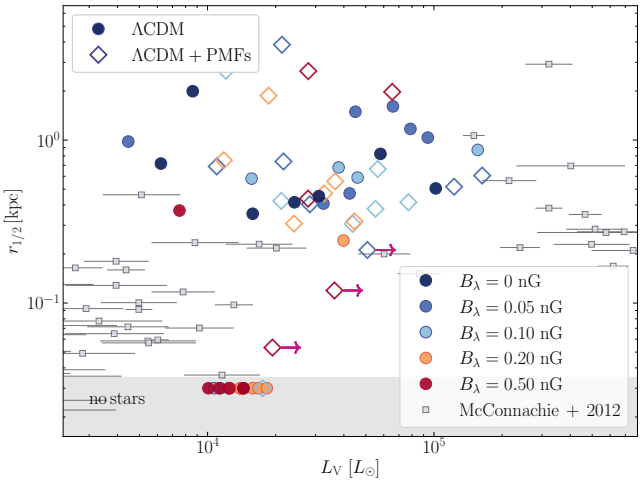

Fig. 9. Half-light radius as a function of V-band luminosity of each model galaxy at redshift $z = 0$ is compared to Milky Way and M 31 satellites in black squares, given by McConnachie (2012). In order to include six halos which do not form any stars in the plot, their luminosities are shown at $L_V \sim 10^3\,L_\odot$.

and size. The half-light sizes in this model span approximately from 300 to 850 pc.

Galaxies in the first set of simulations, ΛCDM, are represented by colored circles. Here, the influence of magnetic fields correlates with the half-light radius of the simulated galaxies. The more compact the galaxies, the less effect magnetic fields have on their gas distribution and, consequently, on their star formation. A magnetic field strength of $B_\lambda = 0.05$ nG in the majority of galaxies in our sample increases the half-light radius by an average value of 25%. However, for $B_\lambda > 0.05$ nG, magnetic fields hinder star formation in small minihalos and by preventing the formation of stars in the outskirts, shrink the size of ultra-faint dwarf galaxies. It demonstrates that incorporating magnetic fields of strength $B_\lambda > 0.05$ nG and $B_\lambda < 0.50$ nG in hydrodynamical simulations leads to a reduction in the size of dwarf galaxies, offering a plausible mechanism for the formation of very compact ultra-faint dwarfs (see e.g., Revaz 2023 for a detailed discussion on reproducing compact ultra-faint dwarf galaxies).

Simulated dwarfs in the second set of simulations, ΛCDM+PMFs, are represented by colored empty diamonds. In these models, the stellar half-mass is more widely dispersed within the halo of each galaxy. This is a direct consequence of the primordial magnetic fields, which increase the stellar line-of-sight velocity dispersion. Here, stars form in more abundant subhalos and will be brought to the main halo of the galaxy by mergers. This results in an increased kinematic energy component and higher velocity dispersion (Revaz 2023). The large angular momenta of these merging subhalos imply larger sizes for the simulated dwarf galaxies. This effect becomes especially pronounced when $B_\lambda = 0.20$ and 0.50 nG.

To summarize, the $z = 0$ properties of halos formed in our fiducial model, provide a good representation of spheroidal and ultra-faint dwarf galaxies in the Local Group, serving as a robust basis for predicting the influence of magnetic fields. From our findings, we can affirm that primordial magnetic fields with strengths $B_\lambda \geq 0.05$ nG significantly impact the physical observables of dwarf galaxies, specially the small mass ultra-faints with luminosities below $10^5\,L_\odot$. In this work, the best consistency with the scaling relations of Local Group dwarfs in our simulated galaxies is obtained when incorporating primordial magnetic fields with moderate strengths of $B_\lambda = 0.05$ and 0.10 nG in the MHD configuration.

5. Discussion and conclusions

In this study, we investigate the impact of primordial magnetic fields on the formation and evolution of dwarf galaxies. We conducted new cosmological zoom-in magneto-hydrodynamical simulations from redshift $z = 200$ to zero. These simulations are focused on eight halos that host dwarfs with V-band luminosities ranging from approximately 10^3 to $10^6\,L_\odot$. All simulations are generated using our modified version of the constrained transport MHD RAMSES code.

We employed two different simulation setups. In the first setup, a uniform magnetic field is initialized with a given

strength and the matter power spectrum follows the classical ΛCDM paradigm. In the second setup, we explored the impact of both varying magnetic field strengths and including the effect of a Gaussian random primordial magnetic field on the matter distribution. This approach allowed us to examine the combined effect of primordial magnetic fields on the matter power spectrum, on the one hand, and the influence of magneto-hydrodynamics on the evolution of small mass galaxies, on the other hand.

Depending on the strength, each magnetic field model affects a distinct mass range of dark matter halos, within the mass range relevant to host halos of dwarf galaxies. In this study, we explored a range of primordial magnetic fields with varying strengths, specifically in the range $B_\lambda = 0.05{-}0.50\,\mathrm{nG}$, while keeping the spectral index constant at $n_B = -2.9$. All of these magnetic field strengths fall within the limits allowed by cosmological constraints listed in Section 1. Our main results can be summarized as follows:

- In the context of a ΛCDM cosmological framework, magnetic fields with an initial strength of $B_\lambda \geq 0.05\,\mathrm{nG}$, have a non-negligible contribution in shaping the evolution of dwarf galaxies. These fields not only delay the collapse of gas clouds, but in the presence of $B_\lambda \geq 0.20\,\mathrm{nG}$ prevent the formation of dense gas minihalos altogether. This effect is stronger in low-mass ultra-faint dwarf galaxies with halo mass and stellar mass below $M_{200} \sim 2.5 \times 10^9\,M_\odot$ and $M_\star \sim 3 \times 10^6\,M_\odot$, respectively, due to the shallow potential well of their host halos.
- In a cosmological setup evolved from initial conditions of ΛCDM+PMFs, the main halo of a dwarf galaxy, as well as the number of its subhalos, are influenced. When the halos affected by primordial magnetic fields fall within the Jeans mass range $M_l \leq 10^8\,\mathrm{M}_\odot$, the gas is distributed among a higher number of these low-mass subhalos. On the other hand, if the halo mass range affected contains the Jeans mass of the main halo of a dwarf galaxy ($M_l \simeq 10^9\,\mathrm{M}_\odot$), the gas content in the central halo increases. This strong gravitational potential can lead to the merging of satellite subhalos and ultimately increase the final mass of the host galaxy.
- Following the delay caused by magnetic fields during the formation of first stars, the gravitational field of low-mass dark matter halos is unlikely to retain gas when it is pushed out by UV-radiation during the epoch of reionisation. This results in the depletion of the gas reservoir in minihalos and an earlier quenching of star formation. In our sample, the density and temperature of gas in all six ultra-faint halos remain below the MTT criteria to form stellar particles. However, the influence of primordial magnetic fields on the matter power spectrum accelerates the formation of the first dark matter minihalos, leading to an earlier onset and a higher rate of star formation at redshifts $z > 12$.
- The observable properties of dwarf galaxies at redshift $z = 0$ are indicative of the influence of magnetic fields on their star formation history and kinematics. Comparing the two simulation setups, we observe that dwarf galaxies forming in a ΛCDM+PMFs Universe with a moderate primordial magnetic field of $B_\lambda = 0.05$ and $0.10\,\mathrm{nG}$ are more consistent with the scaling relations of Local Group observations. However, stronger magnetic fields lead to dwarf galaxies with larger size and higher velocity dispersion compared to the observed Milky Way satellites.
- Increasing the strength of magnetic fields does not result in a proportional $B_\lambda^2/8\pi$ increase in magnetic energy. This suggests energy loss due to magnetic field saturation, with some energy dissipation even occurring during the collapse phase. The saturation of magnetic energy occurs more rapidly when $B_\lambda \geq 0.20\,\mathrm{nG}$, within relatively short time intervals of a few hundred Myr. When $B_\lambda \leq 0.10\,\mathrm{nG}$, it takes a longer time for the magnetic energy to reach saturation.
- In our simulations, the buildup of magnetic energy in time differs from the evolution of magnetic fields in an adiabatic spherical collapse with magnetic flux freezing, also referred to as compressional amplification. This latter is not driven by the supernovae feedback, suggesting that the amplification of the magnetic energy is not provoked in the course of supernovae explosions. Instead, it supports the growth of magnetic fields initialized with a seed as small as $B_\lambda = 0.05\,\mathrm{nG}$ due to dynamo amplification.

In summary, primordial magnetic fields have a substantial impact on the initial stages of dwarf galaxy formation by modifying the matter power spectrum. Moreover, magnetic fields play an important role in the evolution of dwarf galaxies by contributing to the ISM energy budget. These effects set dwarf galaxies apart as an unprecedented window into primordial magnetism. Therefore, the interplay between simulations and observations of spheroidal and ultra-faint dwarf galaxy populations has the potential to further constrain and inform our understanding of the primordial magnetic fields in our Universe. On the other hand, the early structure formation induced by primordial magnetic fields is potentially capable of producing rapid and efficient star formation at high redshifts, as suggested by the JWST data.

Acknowledgements. This work was performed using the DiRAC Data Intensive service at Leicester, operated by the University of Leicester IT Services, which forms part of the STFC DiRAC HPC Facility (www.dirac.ac.uk). The equipment was funded by BEIS capital funding via STFC capital grants ST/K000373/1 and ST/R002363/1 and STFC DiRAC Operations grant ST/R001014/1. DiRAC is part of the National e-Infrastructure. M.S. acknowledges the support from the Swiss National Science Foundation under Grant No. P500PT_214488. J.S. acknowledges the support from the Swiss National Science Foundation under Grant No. 185863. S.M.A. acknowledges support from the Kavli Institute for Particle Astrophysics and Cosmology (KIPAC) Fellowship and by the NASA/DLR Stratospheric Observatory for Infrared Astronomy (SOFIA) under the 08_0012 Program. SOFIA is jointly operated by the Universities Space Research Association, Inc. (USRA), under NASA contract NNA17BF53C, and the Deutsches SOFIA Institut (DSI) under DLR contract 50OK0901 to the University of Stuttgart.

References

Acciari, V. A., Agudo, I., Aniello, T., et al. 2023, A&A, 670, A145
Ackermann, M., Ajello, M., Baldini, L., et al. 2018, ApJS, 237, 32
Adshead, P., Giblin, J. T., Scully, T. R., & Sfakianakis, E. I. 2016, JCAP, 2016, 039
Agertz, O., Pontzen, A., Read, J. I., et al. 2020, MNRAS, 491, 1656
Aharonian, F., Aschersleben, J., Backes, M., et al. 2023, ApJ, 950, L16
Alves Batista, R., & Saveliev, A. 2019, JCAP, 2019, 011
Applebaum, E., Brooks, A. M., Christensen, C. R., et al. 2021, ArXiv e-prints [arXiv:2008.11207]
Arámburo-García, A., Bondarenko, K., Boyarsky, A., et al. 2021, MNRAS, 505, 5038
Archambault, S., & VERITAS Collaboration 2017, Int. Cosm. Ray Conf., 301, 691
Asada, Y., Sawicki, M., Abraham, R., et al. 2024, MNRAS, 527, 11372
Basu, A., & Roy, S. 2013, MNRAS, 433, 1675
Battaglia, G., Helmi, A., Tolstoy, E., et al. 2008, ApJ, 681, L13
Beck, R. 2001, Space Sci. Rev., 99, 243
Beck, R. 2015a, A&A, 578, A93
Beck, R. 2015b, A&ARv, 24, 4
Beck, R., & Wielebinski, R. 2013, in Magnetic Fields in Galaxies, eds. T. D. Oswalt, & G. Gilmore, 5, 641
Behroozi, P. S., Wechsler, R. H., & Conroy, C. 2013, ApJ, 770, 57
Bernet, M. L., Miniati, F., Lilly, S. J., Kronberg, P. P., & Dessauges-Zavadsky, M. 2008, Nature, 454, 302

Bertone, S., Vogt, C., & Enßlin, T. 2006, MNRAS, 370, 319
Biermann, L. 1950, Zeitschrift Naturforschung Teil A, 5, 65
Binggeli, B., Sandage, A., & Tammann, G. A. 1985, AJ, 90, 1681
Borlaff, A. S., Lopez-Rodriguez, E., Beck, R., et al. 2023, ApJ, 952, 4
Boylan-Kolchin, M., Bullock, J. S., & Kaplinghat, M. 2011, MNRAS, 415, L40
Boylan-Kolchin, M., Bullock, J. S., & Kaplinghat, M. 2012, MNRAS, 422, 1203
Bray, J. D., & Scaife, A. M. M. 2018, ApJ, 861, 3
Bromm, V., & Loeb, A. 2003, Nature, 425, 812
Brown, T. M., Tumlinson, J., Geha, M., et al. 2014, ApJ, 796, 91
Bullock, J. S., & Boylan-Kolchin, M. 2017, ARA&A, 55, 343
Caprini, C., Durrer, R., & Servant, G. 2009, JCAP, 2009, 024
Carretti, E., Vacca, V., O'Sullivan, S. P., et al. 2022, MNRAS, 512, 945
Cheera, V., & Nigam, R. 2018, Ap&SS, 363, 93
Clarke, T. E., Kronberg, P. P., & Böhringer, H. 2001, ApJ, 547, L111
Dodelson, S. 2003, Modern Cosmology (Elsevier)
Domcke, V., von Harling, B., Morgante, E., & Mukaida, K. 2019, JCAP, 2019, 032
Durrer, R. 2007, New Astron. Rev., 51, 275
Durrer, R., & Neronov, A. 2013, A&ARv, 21, 62
Ellis, J., Fairbairn, M., Lewicki, M., Vaskonen, V., & Wickens, A. 2019, JCAP, 2019, 019
Escala, I., Wetzel, A., Kirby, E. N., et al. 2018, MNRAS, 474, 2194
Fabrizio, M., Nonino, M., Stetson, P. B., et al. 2011, EAS Publ. Ser., 48, 81
Fabrizio, M., Bono, G., Nonino, M., et al. 2016, ApJ, 830, 126
Federrath, C., & Klessen, R. S. 2012, ApJ, 761, 156
Ferland, G. J., Korista, K. T., Verner, D. A., et al. 1998, PASP, 110, 761
Finkelstein, S. L., Leung, G. C. K., Bagley, M. B., et al. 2024, ArXiv e-prints [arXiv:2311.04279]
Fletcher, A., Beck, R., Shukurov, A., Berkhuijsen, E. M., & Horellou, C. 2011, MNRAS, 412, 2396
Fromang, S., Hennebelle, P., & Teyssier, R. 2006, A&A, 457, 371
Fujita, T., & Durrer, R. 2019, JCAP, 2019, 008
Furlanetto, S. R., & Loeb, A. 2001, ApJ, 556, 619
Gallart, C., Monelli, M., Ruiz-Lara, T., et al. 2021, ApJ, 909, 192
Galli, S., Pogosian, L., Jedamzik, K., & Balkenhol, L. 2022, Phys. Rev. D, 105, 023513
Garnett, D. R. 2002, ApJ, 581, 1019
Geach, J. E., Lopez-Rodriguez, E., Doherty, M. J., et al. 2023, Nature, 621, 483
Gelli, V., Salvadori, S., Ferrara, A., Pallottini, A., & Carniani, S. 2021, ApJ, 913, L25
Gnedin, N. Y., Ferrara, A., & Zweibel, E. G. 2000, ApJ, 539, 505
Gopal, R., & Sethi, S. K. 2003, JApA, 24, 51
Govoni, F., & Feretti, L. 2004, Int. J. Mod. Phys. D, 13, 1549
Govoni, F., Orrù, E., Bonafede, A., et al. 2019, Science, 364, 981
Grønnow, A., Tepper-García, T., & Bland-Hawthorn, J. 2018, ApJ, 865, 64
Groves, B. A., Cho, J., Dopita, M., & Lazarian, A. 2003, PASA, 20, 252
Gutcke, T. A., Pakmor, R., Naab, T., & Springel, V. 2021, MNRAS, 501, 5597
Haardt, F., & Madau, P. 1996, ApJ, 461, 20
Hahn, O., & Abel, T. 2011, MNRAS, 415, 2101
Hanayama, H., Takahashi, K., Kotake, K., et al. 2005, ApJ, 633, 941
Harrison, E. R. 1970, Phys. Rev. D, 1, 2726
Hogan, C. J. 1983, Phys. Lett. B, 133, 172
Hopkins, P. F., & Raives, M. J. 2016, MNRAS, 455, 51
Hopkins, P. F., Wetzel, A., Wheeler, C., et al. 2023, MNRAS, 519, 3154
Ichiki, K., & Takahashi, K. 2006, Astron. Herald, 99, 568
Iffrig, O., & Hennebelle, P. 2017, A&A, 604, A70
Inoue, S., & Yoshida, N. 2019, MNRAS, 485, 3024
Jedamzik, K., & Pogosian, L. 2020, Phys. Rev. Lett., 125, 181302
Jedamzik, K., Katalinić, V., & Olinto, A. V. 1998, Phys. Rev. D, 57, 3264
Jeon, M., & Bromm, V. 2019, MNRAS, 485, 5939
Jeon, M., Besla, G., & Bromm, V. 2017, ApJ, 848, 85
Joyce, M., & Shaposhnikov, M. 1997, Phys. Rev. Lett., 79, 1193
Kandus, A., Kunze, K. E., & Tsagas, C. G. 2011, Phys. Rep., 505, 1
Katz, H., Martin-Alvarez, S., Rosdahl, J., et al. 2021, MNRAS, 507, 1254
Kernan, P. J., Starkman, G. D., & Vachaspati, T. 1996, Phys. Rev. D, 54, 7207
Kim, E.-J., Olinto, A. V., & Rosner, R. 1996, ApJ, 468, 28
Kimm, T., & Cen, R. 2014, ApJ, 788, 121
Kimm, T., Katz, H., Haehnelt, M., et al. 2017, MNRAS, 466, 4826
Knebe, A., Wagner, C., Knollmann, S., Diekershoff, T., & Krause, F. 2009, ApJ, 698, 266
Körtgen, B., Banerjee, R., Pudritz, R. E., & Schmidt, W. 2019, MNRAS, 489, 5004
Koudmani, S., Sijacki, D., & Smith, M. C. 2022, MNRAS, 516, 2112
Kroupa, P. 2001, MNRAS, 322, 231
Krumholz, M. R., & Federrath, C. 2019, Front. Astron. Space Sci., 6, 7
Kulsrud, R. M., Cen, R., Ostriker, J. P., & Ryu, D. 1997, ApJ, 480, 481
Lequeux, J., Peimbert, M., Rayo, J. F., Serrano, A., & Torres-Peimbert, S. 1979, A&A, 500, 145
Lopez-Rodriguez, E., Borlaff, A. S., Beck, R., et al. 2023, ApJ, 942, L13
Ma, X., Hopkins, P. F., Garrison-Kimmel, S., et al. 2018, MNRAS, 478, 1694
Macciò, A. V., Frings, J., Buck, T., et al. 2017, MNRAS, 472, 2356
Mao, S. A., Carilli, C., Gaensler, B. M., et al. 2017, Nat. Astron., 1, 621
Martin-Alvarez, S., Devriendt, J., Slyz, A., & Teyssier, R. 2018, MNRAS, 479, 3343
Martin-Alvarez, S., Slyz, A., Devriendt, J., & Gómez-Guijarro, C. 2020, MNRAS, 495, 4475
Martin-Alvarez, S., Katz, H., Sijacki, D., Devriendt, J., & Slyz, A. 2021, MNRAS, 504, 2517
Martin-Alvarez, S., Devriendt, J., Slyz, A., et al. 2022, MNRAS, 513, 3326
Martin-Alvarez, S., Sijacki, D., Haehnelt, M. G., et al. 2023, MNRAS, 525, 3806
McBride, J., & Heiles, C. 2013, ApJ, 763, 8
McConnachie, A. W. 2012, AJ, 144, 4
Moster, B. P., Naab, T., & White, S. D. M. 2013, MNRAS, 428, 3121
Mtchedlidze, S., Domínguez-Fernández, P., Du, X., et al. 2023, ArXiv e-prints [arXiv:2210.10183]
Naoz, S., & Narayan, R. 2013, Phys. Rev. Lett., 111, 051303
Neronov, A., & Vovk, I. 2010, Science, 328, 73
Okamoto, S., Arimoto, N., Yamada, Y., & Onodera, M. 2012, ApJ, 744, 96
Oman, K. A., Navarro, J. F., Fattahi, A., et al. 2015, MNRAS, 452, 3650
Oñorbe, J., Garrison-Kimmel, S., Maller, A. H., et al. 2014, MNRAS, 437, 1894
Oñorbe, J., Boylan-Kolchin, M., Bullock, J. S., et al. 2015, MNRAS, 454, 2092
O'Sullivan, S. P., Brüggen, M., Vazza, F., et al. 2020, MNRAS, 495, 2607
Padoan, P., & Nordlund, Å. 2011, ApJ, 730, 40
Pakmor, R., Gómez, F. A., Grand, R. J. J., et al. 2017, MNRAS, 469, 3185
Pandey, K. L., & Sethi, S. K. 2012, ApJ, 748, 27
Pandey, K. L., & Sethi, S. K. 2013, ApJ, 762, 15
Pandey, K. L., Choudhury, T. R., Sethi, S. K., & Ferrara, A. 2015, MNRAS, 451, 1692
Patel, S. G., Kelson, D. D., Diao, N., Tonnesen, S., & Abramson, L. E. 2018, ApJ, 866, L21
Pawlowski, M. S., & Kroupa, P. 2013, MNRAS, 435, 2116
Peebles, P. J. E. 1980, The Large-Scale Structure of the Universe (Princeton: Princeton University Press)
Peebles, P. J. E., & Yu, J. T. 1970, ApJ, 162, 815
Planck Collaboration XIII. 2016, A&A, 594, A13
Planck Collaboration XLVII. 2016, A&A, 596, A108
Prgomet, M., Rey, M. P., Andersson, E. P., et al. 2022, MNRAS, 513, 2326
Rasera, Y., & Teyssier, R. 2006, A&A, 445, 1
Ratra, B. 1992, ApJ, 391, L1
Reiners, A. 2012, Liv. Rev. Sol. Phys., 9, 1
Relatores, N. C., Newman, A. B., Simon, J. D., et al. 2019, ApJ, 887, 94
Revaz, Y. 2023, A&A, 679, A2
Revaz, Y., & Jablonka, P. 2018, A&A, 616, A96
Rieder, M., & Teyssier, R. 2017a, MNRAS, 471, 2674
Rieder, M., & Teyssier, R. 2017b, MNRAS, 472, 4368
Robishaw, T., Quataert, E., & Heiles, C. 2008, ApJ, 680, 981
Rosen, A., & Bregman, J. N. 1995, ApJ, 440, 634
Ryu, D., Kang, H., & Biermann, P. L. 1998, A&A, 335, 19
Ryu, D., Kang, H., Cho, J., & Das, S. 2008, Science, 320, 909
Sacchi, E., Richstein, H., Kallivayalil, N., et al. 2021, ApJ, 920, L19
Safarzadeh, M. 2018, MNRAS, 479, 315
Sales, L. V., Wetzel, A., & Fattahi, A. 2022, Nat. Astron., 6, 897
Sanati, M., Revaz, Y., Schober, J., Kunze, K. E., & Jablonka, P. 2020, A&A, 643, A54
Sanati, M., Jeanquartier, F., Revaz, Y., & Jablonka, P. 2023, A&A, 669, A94
Schmidt, M. 1959, ApJ, 129, 243
Schober, J., Schleicher, D. R. G., & Klessen, R. S. 2013, A&A, 560, A87
Schober, J., Rogachevskii, I., & Brandenburg, A. 2022, Phys. Rev. D, 105, 043507
Seshadri, T. R., & Subramanian, K. 2009, Phys. Rev. Lett., 103, 081303
Sethi, S. K., & Subramanian, K. 2005, MNRAS, 356, 778
Shaw, J. R., & Lewis, A. 2010, Phys. Rev. D, 81, 043517
Shaw, J. R., & Lewis, A. 2012, Phys. Rev. D, 86, 043510
Simon, J. D. 2019, ARA&A, 57, 375
Sironi, L., Comisso, L., & Golant, R. 2023, Phys. Rev. Lett., 131, 055201
Skillman, E. D., Kennicutt, R. C., & Hodge, P. W. 1989, ApJ, 347, 875
Stevenson, D. J. 2010, Space Sci. Rev., 152, 651
Su, K.-Y., Hopkins, P. F., Hayward, C. C., et al. 2020, MNRAS, 491, 1190
Subramanian, K. 2016, Rep. Progr. Phys., 79, 076901
Subramanian, K., & Barrow, J. D. 1998, Phys. Rev. Lett., 81, 3575
Subramanian, K., Narasimha, D., & Chitre, S. M. 1994, MNRAS, 271, L15
Subramanian, K., Shukurov, A., & Haugen, N. E. L. 2006, MNRAS, 366, 1437
Sur, S., Federrath, C., Schleicher, D. R. G., Banerjee, R., & Klessen, R. S. 2012, MNRAS, 423, 3148
Tashiro, H., Silk, J., Langer, M., & Sugiyama, N. 2009, MNRAS, 392, 1421

Tavecchio, F., Ghisellini, G., Bonnoli, G., & Foschini, L. 2011, MNRAS, 414, 3566
Taylor, A. M., Vovk, I., & Neronov, A. 2011, A&A, 529, A144
Tegmark, M., & Zaldarriaga, M. 2002, Phys. Rev. D, 66, 103508
Teyssier, R. 2002, A&A, 385, 337
Teyssier, R., Fromang, S., & Dormy, E. 2006, J. Comput. Phys., 218, 44
Tjemsland, J., Meyer, M., & Vazza, F. 2024, ArXiv e-prints [arXiv:2311.04273]
Tóth, G. 2000, J. Comput. Phys., 161, 605
Trebitsch, M., Blaizot, J., Rosdahl, J., Devriendt, J., & Slyz, A. 2017, MNRAS, 470, 224
Tremonti, C. A., Heckman, T. M., Kauffmann, G., et al. 2004, ApJ, 613, 898
Trivedi, P., Seshadri, T. R., & Subramanian, K. 2012, Phys. Rev. Lett., 108, 231301
Trivedi, P., Subramanian, K., & Seshadri, T. R. 2014, Phys. Rev. D, 89, 043523
Tsagas, C. G., & Maartens, R. 2000, Phys. Rev. D, 61, 083519
Turner, M. S., & Widrow, L. M. 1988, Phys. Rev. D, 37, 2743
van de Voort, F., Bieri, R., Pakmor, R., et al. 2021, MNRAS, 501, 4888
Varalakshmi, C., & Nigam, R. 2017, Ap&SS, 362, 16
Vazdekis, A., Casuso, E., Peletier, R. F., & Beckman, J. E. 1996, ApJS, 106, 307
Vazza, F., Brüggen, M., Gheller, C., & Wang, P. 2014, MNRAS, 445, 3706
Vazza, F., Brüggen, M., Gheller, C., et al. 2017, Class. Quant. Grav., 34, 234001
Vazza, F., Brunetti, G., Brüggen, M., & Bonafede, A. 2018, MNRAS, 474, 1672
Vogt, C., & Enßlin, T. A. 2005, A&A, 434, 67
Walker, M. G., Mateo, M., & Olszewski, E. W. 2009, AJ, 137, 3100
Wasserman, I. M. 1978a, Ph.D. Thesis, Harvard University, USA
Wasserman, I. 1978b, ApJ, 224, 337
Wheeler, C., Hopkins, P. F., Pace, A. B., et al. 2019, MNRAS, 490, 4447
Widrow, L. M. 2002, Rev. Mod. Phys., 74, 775
Widrow, L. M., Ryu, D., Schleicher, D. R. G., et al. 2012, Space Sci. Rev., 166, 37
Wolfe, A. M., Lanzetta, K. M., & Oren, A. L. 1992, ApJ, 388, 17
Yajima, H., Abe, M., Fukushima, H., et al. 2023, ArXiv e-prints [arXiv:2211.12970]
Zamora-Avilés, M., Vázquez-Semadeni, E., Körtgen, B., Banerjee, R., & Hartmann, L. 2018, MNRAS, 474, 4824
Zeldovich, Y. B. 1972, MNRAS, 160, 1P
Zhou, M., Zhdankin, V., Kunz, M. W., Loureiro, N. F., & Uzdensky, D. A. 2024, ApJ, 960, 12